

# Verification of the Effectiveness of VSOP-2 Phase Referencing with a Newly Developed Simulation Tool, ARIS

Yoshiharu ASAKI,<sup>1,2</sup> Hiroshi SUDOU,<sup>3</sup> Yusuke KONO,<sup>4</sup> Akihiro DOI,<sup>5</sup> Richard DODSON,<sup>6</sup>  
Nicolas PRADEL,<sup>4</sup> Yasuhiro MURATA,<sup>1,2</sup> Nanako MOCHIZUKI,<sup>1</sup> Philip G. EDWARDS,<sup>7</sup>  
Tetsuo SASAO,<sup>8</sup>

and

Edward B. FOMALONT<sup>9</sup>

<sup>1</sup> *Institute of Space and Astronautical Science, 3-1-1 Yoshinodai, Sagamihara, Kanagawa 229-8510*

<sup>2</sup> *Department of Space and Astronautical Science, School of Physical Sciences,  
The Graduate University for Advanced Studies, 3-1-1 Yoshinodai, Sagamihara, Kanagawa 229-8510*

<sup>3</sup> *Department of Mathematical and Design Engineering, Faculty of Engineering, Gifu University,  
1-1 Yanagido, Gifu, Gifu 501-1193*

<sup>4</sup> *National Astronomical Observatory, 2-21-1 Osawa, Mitaka, Tokyo 181-8588*

<sup>5</sup> *Department of Physics, Faculty of Science, Yamaguchi University,  
1677-1 Yoshida, Yamaguchi, Yamaguchi 753-8511*

<sup>6</sup> *Observatorio Astronomico Nacional, Apartado 112 E-28803 Alcala de Henares Spain*

<sup>7</sup> *Australia Telescope National Facility, CSIRO, Locked Bag 194 Narrabri NSW 2390 Australia*

<sup>8</sup> *Korea Astronomy and Space Science Institute, 61-1 Hwaam-dong, Yuseong-gu, Daejeon 305-348 Korea*

<sup>9</sup> *National Radio Astronomy Observatory, 520 Edgemont Road, Charlottesville, VA 22903 USA*  
*asaki@vsop.isas.jaxa.jp, sudou@gifu-u.ac.jp, kono.yusuke@nao.ac.jp, doi@yamaguchi-u.ac.jp, r.dodson@oan.es,*  
*nicolas.pradel@nao.ac.jp, murata@vsop.isas.jaxa.jp, nanakom@vsop.isas.jaxa.jp, philip.edwards@csiro.au,*  
*sasao@ajou.ac.kr, efomalon@nrao.edu*

(Received 2006 July 3; accepted 2006 December 25)

## Abstract

The next-generation space VLBI mission, VSOP-2, is expected to provide unprecedented spatial resolutions at 8.4, 22, and 43 GHz. In this report, phase referencing with VSOP-2 is examined in detail based on a simulation tool called ARIS. The criterion for successful phase referencing was to keep the phase errors below one radian. Simulations with ARIS reveal that phase referencing achieves good performance at 8.4 GHz, even under poor tropospheric conditions. At 22 and 43 GHz, it is recommended to conduct phase referencing observations under good or typical tropospheric conditions. The satellite is required to have an attitude-switching capability with a one-minute or shorter cycle, and an orbit determination accuracy higher than  $\sim 10$  cm at apogee; the phase referencing calibrators are required to have a signal-to-noise ratio larger than four for a single scan. The probability to find a suitable phase referencing calibrator was estimated by using VLBI surveys. From the viewpoint of calibrator availability, VSOP-2 phase referencing at 8.4 GHz is promising. However, the change of finding suitable calibrators at 22 and 43 GHz is significantly reduced; it is important to conduct specific investigations for each target at those frequencies.

**Key words:** instrumentation: high angular resolution— space vehicles: instruments— techniques: image processing

## 1. Introduction

A series of space Very Long Baseline Interferometry (VLBI) experiments in which an orbiting radio telescope satellite was used for VLBI observations has provided successful development of very high spatial resolution in astronomy. In particular, the first dedicated space VLBI project, VSOP, with the HALCA satellite achieved remarkable scientific results based on spatial resolution up to 1.2 and 0.4 mas at 1.6 and 5 GHz, respectively, with an apogee altitude of 21375 km (Hirabayashi et al. 1998). To come after the successful VSOP, the next space VLBI mission, VSOP-2, is being planned by Institute of Space and Astronautical Science (ISAS) (Hirabayashi et al. 2004).

This project will launch a satellite radio telescope (SRT), which will be equipped with a 9.1-m off-axis paraboloid antenna and dual-polarization receivers to observe at 8.4, 22, and 43 GHz, together with terrestrial radio telescopes (TRTs) with the sensitivity being a factor-of-ten higher than VSOP. Launch is planned for 2012. With two intermediate frequency (IF) bands, each with a two-bit sampled 128-MHz a total 256-MHz bandwidth will be available. The achievable maximum baselines will exceed 37800 km with the planned apogee altitude of 25000 km, and the highest spatial resolution will be  $38 \mu\text{as}$  at 43 GHz.

Millimeter-wave observations in space VLBI will be a frontier in astrophysics because there are various compact objects for which very high spatial resolution is essential

(Murphy et al. 2005). There is, however, a difficulty in millimeter-wave VLBI in terms of the fringe phase stability. Data-averaging of the fringe is usually performed within a certain time scale, the so-called coherence time, for which a root-mean-square (RMS) of the fringe phase is less than one radian. In the conventional calibration scheme in VLBI with a fringe-fitting technique (Cotton 1995), it is necessary that the fringe be detected in less than the coherence time. The coherence time in VLBI at 43 GHz is limited to a few minutes by stochastic variations in the fringe phase, mainly due to the turbulent media of the Earth's atmosphere; it is thus difficult to conduct a long-time averaging in VLBI in order to improve the signal-to-noise ratio (SNR). Although celestial radio waves received on a satellite are not affected by the atmosphere, the fringe of a space baseline (a combination of orbiting and terrestrial telescopes) also suffers from the atmospheric phase fluctuations because one of the elements is inevitably a terrestrial radio telescope.

Phase referencing is a successful phase-calibration scheme for VLBI. Here a scientifically interesting target source is observed with an adjacent reference calibrator with fast antenna pointing changes (antenna switching) in order to compensate for any rapid phase fluctuations due to the atmosphere (Beasley, Conway 1995; Fomalont 1995). Phase referencing can also remove long-term phase drifts due to geometrical errors and smoothly variable atmospheric delay errors, as well as any instability of the independent frequency standards. The phase referencing technique has been proved for imaging faint radio sources that cannot be detected with the conventional VLBI data reduction (Smith et al. 2003; Gallimore, Beswick 2004; Gallimore et al. 2004). Various astrometric observations in the VLBI field have also been made with the phase referencing technique to obtain the relative positions with the accuracies on the order of  $10 \mu\text{as}$  (Shapiro et al. 1979; Bartel et al. 1986; Gwinn et al. 1986; Lestrade et al. 1990; Reid et al. 1999; Brunthaler et al. 2005).

Phase referencing will be useful for VSOP-2. To investigate which component of errors has a more significant influence than others on the quality of the synthesized images obtained with VSOP-2 phase referencing, and to give feedback for designing the satellite system, a software simulation tool for space VLBI has been developed. Here we report on the effectiveness of VSOP-2 phase referencing by simulation. The basic ideas of phase compensation with phase referencing are described in section 2. The residual phase errors after phase compensation are discussed in section 3 based on quantitative estimations. In section 4, the newly developed space VLBI simulator for this study is described. Simulation work for VSOP-2 phase referencing is presented to clarify the constraints on specific observing parameters: the separation angle between a target and a calibrator; the time interval to switch a pair of sources; the orbit determination accuracy of the satellite. Further discussions are given in section 5 to describe the feasibility of phase referencing with VSOP-2. The conclusions are summarized in section 6.

## 2. Basic Ideas of VLBI Phase Referencing

In this section we describe basic ideas of phase referencing. In the following discussion a single on-source duration is referred to as a scan. In phase referencing, alternate scans are made on the target and phase referencing calibrator. One observation period from the beginning of the calibrator scan, then the target scan and return to the beginning of the calibrator scan, is referred to as the switching cycle time,  $T_{\text{swt}}$ . Figure 1 shows a schematic drawing of VSOP-2 phase referencing. The correlated VLBI data reveal a time series of a complex quantity, called a fringe, which is composed of amplitude and phase including information on the visibility of a celestial object as well as various errors from instruments and propagation media. Let us assume that the difference in the arrival time of a celestial radio wave between telescopes and its derivative are largely removed by subtracting their a priori values, calculated in the correlator.

Phase referencing is used to observe the target and a closely located calibrator in the sky. We refer to the fringe phases of the target and phase referencing calibrator as  $\Phi^t$  and  $\Phi^c$ , respectively, expressed as follows:

$$\begin{aligned} \Phi^t(t^t) - \Phi_{\text{apri}}^t(t^t) &= \Phi_{\text{dtrp}}^t(t^t) + \Phi_{\text{dion}}^t(t^t) + \Phi_{\text{strp}}^t(t^t) \\ &+ \Phi_{\text{sion}}^t(t^t) + \Phi_{\text{bl}}^t(t^t) + \Phi_{\text{inst}}^t(t^t) \\ &+ \Phi_{\Delta_s}^t(t^t) + \Phi_v^t(t^t) + \epsilon_{\text{therm}}^t(t^t), \quad (1) \end{aligned}$$

$$\begin{aligned} \Phi^c(t^c) - \Phi_{\text{pred}}^c(t^c) &= \Phi_{\text{dtrp}}^c(t^c) + \Phi_{\text{dion}}^c(t^c) + \Phi_{\text{strp}}^c(t^c) \\ &+ \Phi_{\text{sion}}^c(t^c) + \Phi_{\text{bl}}^c(t^c) + \Phi_{\text{inst}}^c(t^c) \\ &+ \Phi_{\Delta_s}^c(t^c) + \Phi_v^c(t^c) + \epsilon_{\text{therm}}^c(t^c), \quad (2) \end{aligned}$$

where

$\Phi_{\text{apri}}$  : the a priori phase calculated in the correlator;

$\Phi_{\text{dtrp}}, \Phi_{\text{dion}}$  : phase errors due to the dynamic components of the troposphere and ionosphere, respectively;

$\Phi_{\text{strp}}, \Phi_{\text{sion}}$  : long-term phase variations depending on the observing elevations of terrestrial telescopes due to the uncertainties of the tropospheric and ionospheric zenith excess path delays, respectively;

$\Phi_{\text{bl}}$  : phase error due to the baseline vector error coming from uncertainties of the telescope positions and erroneous estimations of the Earth Orientation Parameters (EOP);

$\Phi_{\text{inst}}$  : the instrumental phase error due to the independent frequency standards, transmitting electric cables and so on;

$\Phi_{\Delta_s}$  : phase error due to the uncertainty in the a priori source position in the sky;

$\Phi_v$  : visibility phase component representing the source structure;

$\epsilon_{\text{therm}}$  : a contribution of the thermal noise.

Here,  $t^t$  is the time that the target is observed, and  $t^c$ , temporally  $T_{\text{swt}}/2$  apart from  $t^t$ , is the time that the calibrator is observed.

If the structure of the calibrator is well-known, three terms can be identified in equation (2), as follows:

$$\Phi^c(t^c) - \Phi_{\text{apri}}^c(t^c) = \Phi_{\text{err}}^c(t^c) + \Phi_v^c(t^c), \quad (3)$$

where  $\Phi_{\text{err}}^c$  is an error term consisting of  $\Phi_{\text{dtrp}}^c$ ,  $\Phi_{\text{dion}}^c$ ,  $\Phi_{\text{strp}}^c$ ,  $\Phi_{\text{sion}}^c$ ,  $\Phi_{\text{bl}}^c$ ,  $\Phi_{\text{inst}}^c$ ,  $\Phi_{\Delta s}^c$ , and  $\epsilon_{\text{therm}}^c$ . The calibration data,  $\Phi_{\text{cal}}$ , for the target at time  $t^t$  is obtained from  $\Phi_{\text{err}}^c$  of the temporally closest two calibrator scans, as follows:

$$\begin{aligned} \Phi_{\text{cal}}(t^t) &= \frac{\Phi_{\text{err}}^c(t^t - T_{\text{swt}}/2) + \Phi_{\text{err}}^c(t^t + T_{\text{swt}}/2)}{2} \\ &= \Phi_{\text{dtrp}}^c(t^t) + \Phi_{\text{dion}}^c(t^t) + \Phi_{\text{strp}}^c(t^t) \\ &\quad + \Phi_{\text{sion}}^c(t^t) + \Phi_{\text{bl}}^c(t^t) + \Phi_{\text{inst}}^c(t^t) \\ &\quad + \Phi_{\Delta s}^c(t^t) + \epsilon_{\text{therm}}^c(t^t), \end{aligned} \quad (4)$$

where  $\Phi^c(t^t)$  and  $\epsilon_{\text{therm}}^c$  are interpolated calibrator phases at  $t^t$ . The final step of the phase compensation is carried out by subtracting  $\Phi_{\text{cal}}(t^t)$  from equation (1), as follows:

$$\begin{aligned} &\Phi^t(t^t) - \Phi_{\text{apri}}^t(t^t) - \Phi_{\text{cal}}(t^t) \\ &= \Phi_v^t(t^t) + \left[ \Phi_{\Delta s}^t(t^t) - \Phi_{\Delta s}^c(t^t) \right] \\ &\quad + \phi_{\text{dtrp}}(t^t) + \phi_{\text{dion}}(t^t) + \phi_{\text{strp}}(t^t) + \phi_{\text{sion}}(t^t) \\ &\quad + \phi_{\text{bl}}(t^t) + \phi_{\text{inst}}(t^t) + \Delta\epsilon_{\text{therm}}(t^t), \end{aligned} \quad (5)$$

where  $\phi$  is the phase difference between  $\Phi^t$  and  $\Phi^c$ , and  $\Delta\epsilon_{\text{therm}}$  is the phase difference between  $\epsilon_{\text{therm}}^t$  and  $\epsilon_{\text{therm}}^c$ . If  $T_{\text{swt}}$  is short enough (typically, shorter than a few minutes at centimeter to millimeter waves) and the calibrator is located closely enough (typically, within a few degrees), the phase errors, except for the thermal noise, can almost be canceled. An uncanceled term,  $\Phi_{\Delta s}^t(t^t) - \Phi_{\Delta s}^c(t^t)$ , gives the relative position of the target to the calibrator with a typical accuracy of much less than one mas. Another aspect of the advantages of phase referencing is to eliminate the rapid time variation caused by the turbulent atmosphere. This means that the coherence time, which is limited by the atmosphere, becomes longer, so that faint radio sources can be detected by means of the long time averaging.

### 3. Residual Phase Errors after Phase Referencing with VSOP-2

Although phase referencing is capable of removing a large amount of the fringe phase errors, residual phase errors remain after phase compensation because the target and calibrator are observed with a certain time separation, and not on the same line of sight. Being different from a terrestrial baseline consisting of both terrestrial telescopes, a single space baseline includes a single line-of-sight atmospheric phase error for a terrestrial telescope, and uncertainty of a satellite trajectory in the orbit. In this section we analytically estimate the residual phase errors of the space baseline after phase compensation. We attempt to characterize the distribution of phase offsets from a very large number of samples obtained with given parameters, such as uncertainties in the a priori values, switching cycle time, separation angle, zenith angle, and so on.

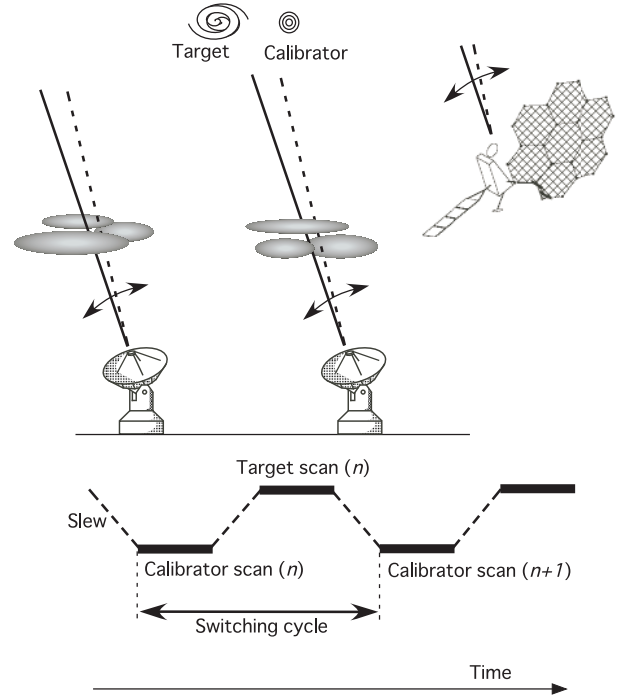


Fig. 1. Schematic drawing of VSOP-2 phase referencing.

#### 3.1. Fringe Phase Fluctuations due to a Turbulent Atmosphere

The Earth's atmosphere causes an excess path of radio waves passing through it (Thompson et al. 2001). Let us distinguish two types of excess path errors in the following discussions: one is a dynamic component (fluctuation error), and the other one is a nearly static component (systematic error). Here, we first address the atmospheric phase fluctuations.

##### 3.1.1. Statistical model of atmospheric phase fluctuations

Phase differences due to a turbulent medium are often characterized by a spatial structure function (SSF), which is defined as the mean-square difference in the phase fluctuations at two sites separated by a displacement vector,  $\rho$ , (Tatarskii 1961) as follows:

$$D(\rho) = \left\langle [\Phi(\mathbf{x} + \rho) - \Phi(\mathbf{x})]^2 \right\rangle, \quad (6)$$

where the angle brackets mean an ensemble average, and  $\mathbf{x}$  is a position vector. According to Dravskikh, Finkelstein (1979), the SSF of the atmospheric phase shift with Kolmogorov turbulence can be approximated by:

$$D(\rho) = C^2 \rho^{\frac{5}{3}} \quad (\rho \leq L_1), \quad (7)$$

$$D(\rho) = C^2 L_1 \rho^{\frac{2}{3}} \quad (L_1 < \rho \leq L_2), \quad (8)$$

$$D(\rho) = C^2 L_1 L_2^{\frac{2}{3}} \quad (\rho > L_2), \quad (9)$$

where  $L_1$  and  $L_2$  are referred as inner and outer scales, respectively, and  $C$  is a structure coefficient.

The spatial structure of the atmospheric phase fluctuations can also be modeled as a phase screen, assuming

frozen flow (Dravskikh, Finkelstein 1979), in which a laminar sheet with a fixed spatial pattern representing the distribution of the turbulent medium, flows at a constant speed. We use the phase screen model in the following discussions about the atmospheric phase fluctuations.

### 3.1.2. Tropospheric phase fluctuations

The water vapor in the troposphere is neither well mixed nor regularly distributed in the lower troposphere, and therefore is not well correlated with the ground-based meteorological parameters. Hence, the water vapor in the troposphere is highly unpredictable. Carilli, Holdaway (1999) observationally showed that the inner and outer scales of the SSF are 1.2 and 6 km, respectively, at their observing site at the Very Large Array. The tropospheric phase fluctuations play a major role in restricting the coherence time to be quite short, especially at millimeter waves, because the refractive index is non-dispersive in centimeter-to-millimeter waves. At higher observing frequency bands, VLBI synthesized images can be improved by removing telescope data whose weather is not good. Thus, to use a large terrestrial telescope network in VLBI is important not only for  $(u, v)$  coverage, but also to have a number of telescopes where the tropospheric conditions are good.

To make a successful phase connection at 22 or 43 GHz by interpolating the calibrator fringe phases, the switching cycle time should be shorter than a few minutes, and the separation angle should be smaller than a few degrees. Assuming such a fast antenna switching observations for such a pair of sources, a residual phase error,  $\sigma_{\phi_{\text{dtrp}}}$ , due to the dynamic troposphere for a space baseline, is expressed as follows:

$$\sigma_{\phi_{\text{dtrp}}} [\text{rad}] \approx \frac{2\pi\nu C_n \sqrt{1.4H_s} \sqrt{\sec Z_g}}{c} \times \left( \frac{v_w T_{\text{swt}}}{2} + H_w \Delta\theta \sec Z_g \right)^{\frac{5}{6}}, \quad (10)$$

where  $\Delta\theta$  is the separation angle between the target and the calibrator,  $\nu$  is the observing frequency,  $c$  is the speed of light,  $C_n$  is the structure coefficient of the SSF of the troposphere to the zenith, defined by Beasley, Conway (1995),  $H_s$  is the scale height of the tropospheric water vapor,  $v_w$  is the wind velocity aloft or flow speed of the phase screen,  $H_w$  is the height of the phase screen, and  $Z_g$  is the zenith angle at the ground surface for a terrestrial telescope. The first  $\sec Z_g$  in equation (10) comes from an indication based on numerical calculations for the tropospheric phase fluctuations made by Treuhaft, Lanyi (1987), while the second comes from a factor to project the separation between a pair of sources onto the phase screen. Although  $C_n$  is very different at different telescope sites, seasons, and weather conditions, it can be assumed that the values of  $1 \times 10^{-7}$ ,  $2 \times 10^{-7}$ , and  $4 \times 10^{-7} \text{ m}^{-1/3}$  are equivalent to good, typical, and poor tropospheric conditions, respectively, with the assumption of Kolmogorov turbulence (J. Ulvestad, VLBA Scientific Memo No.20).<sup>1</sup> Assuming typical values of

$H_s = H_w = 1 \text{ km}$  and  $v_w = 10 \text{ m s}^{-1}$ , we can obtain the following approximation from equation (10):

$$\sigma_{\phi_{\text{dtrp}}} [\text{deg}] \approx 27C_w \cdot \left( \frac{\nu [\text{GHz}]}{43 \text{ GHz}} \right) \left( \frac{\sec Z_g}{\sec 45^\circ} \right)^{\frac{1}{2}} \times \left[ \left( \frac{T_{\text{swt}} [\text{s}]}{60 \text{ s}} \right) + 0.16 \cdot \left( \frac{\sec Z_g}{\sec 45^\circ} \right) \left( \frac{\Delta\theta [\text{deg}]}{2^\circ} \right) \right]^{\frac{5}{6}}, \quad (11)$$

where  $C_w$  is a modified structure coefficient of the SSF, whose values are 1, 2, and 4 for good, typical, and poor tropospheric conditions, respectively. The residual phase errors with the typical parameters used in equation (11) and  $C_w = 2$  are given in table 1.

### 3.1.3. Ionospheric phase fluctuations

Ionospheric phase fluctuations are caused by irregularities of the plasma density in the ionosphere. Since the extra phase due to the Total Electron Content (TEC) has an inverse proportionality to radio frequency, the amplitude of the ionospheric phase fluctuations becomes smaller as the observing frequency increases.

In this report we focus on the temporal TEC variations known as medium-scale traveling ionospheric disturbances (MS-TIDs), which have a severe influence on the VLBI observables, especially at frequencies less than 10 GHz. MS-TIDs, firstly classified by Georges (1968) are often seen at night in high- and mid-latitude areas, and thought to be caused by the thermospheric gravity sound waves at the bottom of the F-region. Studies of spectra of the gravity waves in the high-latitude thermosphere by Bristow, Greenwald (1997) showed that monochromatic waves with a period of a few tens of minutes are present. In addition, the power spectra, ranging from 0.3 to a few milli hertz, show characteristics of Kolmogorov power-law, which indicates that kinematic energy causing the power-law perturbations are injected from the monochromatic gravity sound waves. Typical MS-TIDs in mid-latitudes have a spatial wavelength of a few hundred kilometers and a propagation velocity of around  $100 \text{ ms}^{-1}$  from high- to low-latitudes (Saito et al. 1998).

We here attempt to make a model for ionospheric phase fluctuations with the assumption of a phase screen with Kolmogorov turbulence driven by the MS-TIDs. The residual phase error,  $\sigma_{\phi_{\text{dion}}}$ , due to the dynamic ionosphere for a space baseline, is expressed as follows:

$$\sigma_{\phi_{\text{dion}}} [\text{rad}] \approx \frac{2\pi\kappa C_i \sqrt{\sec Z_i}}{c\nu} \times \left( \frac{v_i T_{\text{swt}}}{2} + H_i \Delta\theta \sec Z_i \right)^{\frac{5}{6}}, \quad (12)$$

where  $\kappa = 40.3 \text{ m}^3 \text{ s}^{-2}$ ,  $C_i$  is the structure coefficient of the SSF of the ionospheric TEC to the zenith,  $v_i$  is the flow speed of the screen, and  $H_i$  is the phase screen height.  $Z_i$  is the zenith angle of the ray at  $H_i$ , as follows:

$$Z_i = \arcsin \left( \frac{R_\oplus}{R_\oplus + H_i} \sin Z_g \right), \quad (13)$$

where  $R_\oplus$  is the Earth radius.

As described in subsection 4.1.1, the value of  $C_i$  for a

<sup>1</sup> <<http://www.vlba.nrao.edu/memos/sci/>>

50-percentile condition is roughly  $1.6 \times 10^{-5}$  TECU·m<sup>-5/6</sup> at mid-latitudes, where TECU is the unit used for TEC (1 TECU =  $10^{16}$  electrons m<sup>-2</sup>). We can obtain the following approximation from equation (12) for the 50-percentile condition with assumptions of  $v_i = 100$  ms<sup>-1</sup> and  $H_i = 300$  km (bottom of the F-region):

$$\sigma_{\phi_{\text{dion}}} [\text{deg}] \approx 0.46 \cdot \left( \frac{\sec Z_i}{\sec 43^\circ} \right)^{\frac{1}{2}} \left( \frac{\nu [\text{GHz}]}{43 \text{ GHz}} \right)^{-1} \times \left[ 0.21 \cdot \left( \frac{T_{\text{swt}} [\text{s}]}{60 \text{ s}} \right) + \left( \frac{\sec Z_i}{\sec 43^\circ} \right) \left( \frac{\Delta\theta [\text{deg}]}{2^\circ} \right) \right]^{\frac{5}{6}}. \quad (14)$$

Note that  $Z_i$  of  $43^\circ$  is the zenith angle at  $H_i = 300$  km when  $Z_g$  is  $45^\circ$ . The residual phase errors with the typical parameters used in equation (14) are shown in table 1.

### 3.2. Static Components of the Troposphere and Ionosphere

Let us focus on the atmospheric excess path errors after subtracting the dynamic components, which we assume to be temporally stable during an observation for up to several hours. The systematic errors are mainly caused by the uncertainty of the tropospheric water vapor constituent, and an inaccurate estimate of vertical TEC (VTEC). Hereafter, the elevation dependence of the atmospheric line-of-sight excess path (mapping function) is approximated by  $\sec Z$  at the height of a homogeneously distributed medium.

The residual phase error,  $\sigma_{\phi_{\text{strp}}}$ , for a space baseline, due to an inaccurate estimate of the tropospheric zenith excess path, is expressed as

$$\sigma_{\phi_{\text{strp}}} [\text{rad}] \approx \frac{2\pi\nu\Delta l_z\Delta Z_g\sec Z_g\tan Z_g}{c}, \quad (15)$$

where  $\Delta l_z$  is the tropospheric systematic error of the excess path length to the zenith, and  $\Delta Z_g$  is a difference of the zenith angles between the target and the calibrator. Assuming a  $\Delta l_z$  of 3 cm (Reid et al. 1999) and  $\Delta Z_g \sim \Delta\theta$ , the following approximation can be obtained from equation (15):

$$\sigma_{\phi_{\text{strp}}} [\text{deg}] \approx 76 \cdot \left( \frac{\nu [\text{GHz}]}{43 \text{ GHz}} \right) \left( \frac{\Delta l_z [\text{cm}]}{3 \text{ cm}} \right) \times \left( \frac{\Delta\theta [\text{deg}]}{2^\circ} \right) \left( \frac{\cos Z_g}{\cos 45^\circ} \right)^{-1} \left( \frac{\tan Z_g}{\tan 45^\circ} \right). \quad (16)$$

The residual phase errors with the typical parameters used in equation (16) are shown in table 1.

A residual phase error  $\sigma_{\phi_{\text{sion}}}$  for a space baseline due to an inaccurate TEC measurement is expressed as follows:

$$\sigma_{\phi_{\text{sion}}} [\text{rad}] \approx \frac{2\pi\kappa\Delta I_v\Delta Z_F\sec Z_F\tan Z_F}{c\nu}, \quad (17)$$

where  $\Delta I_v$  is the VTEC systematic error,  $Z_F$  is the zenith angle at the altitude of the electron density peak (typically, 450 km), and  $\Delta Z_F$  is the difference of the zenith angles between the target and the calibrator. A TEC measurement technique with the Global Positioning System (GPS) has been used to correct for any line-of-sight excess path delays due to the ionosphere (e.g., C. Walker &

S. Chatterjee 1999, VLBA Scientific Memo No.23;<sup>2</sup> Ros et al. 2000). For example, global ionospheric modeling with GPS generally has an accuracy of 3–10 TECU, or at 10–20% level (Ho et al. 1997). Let us assume  $\Delta Z_F \sim \Delta\theta$  and  $Z_g$  of  $45^\circ$  to obtain the following approximation from equation (17):

$$\sigma_{\phi_{\text{sion}}} [\text{deg}] \approx 2.7 \cdot \left( \frac{\nu [\text{GHz}]}{43 \text{ GHz}} \right)^{-1} \times \left( \frac{\Delta I_v [\text{TECU}]}{6 \text{ TECU}} \right) \times \left( \frac{\Delta\theta [\text{deg}]}{2^\circ} \right) \left( \frac{\cos Z_F}{\cos 41^\circ} \right)^{-1} \left( \frac{\tan Z_F}{\tan 41^\circ} \right). \quad (18)$$

The residual phase errors with the typical parameters used in equation (18) are given in table 1.

### 3.3. Baseline Errors

One of the special issues related to the space VLBI is the satellite orbit determination (OD) error. In VSOP, the precisely reconstructed OD of HALCA has an accuracy of 2–5 m (Porcas et al. 2000) with the *S*-band range and range-rate, and the *Ku*-band Doppler measurements, which is the best accuracy achieved by the Doppler tracking. However, the typical accuracy of terrestrial telescope positions is around 1 cm. For VSOP-2, as discussed in subsection 5.3, cm-order OD accuracy will be achieved by using an on-board GPS receiver.

The accuracies of the EOP solutions given by International Earth Rotation and Reference Systems Service (IERS) are typically 0.1 mas in the terrestrial pole offset, 0.3 mas in the celestial pole offset, and 0.02 ms in the UT1 offset. These uncertainties may cause the additional displacement of a few cm for the space baseline. A residual phase error,  $\sigma_{\phi_{\text{bl}}}$ , for a space baseline due to the baseline error is approximated as follows:

$$\sigma_{\phi_{\text{bl}}} [\text{rad}] \approx \frac{\sqrt{2}\pi\nu\Delta\theta}{c} \sqrt{\Delta P_{\text{TRT}}^2 + \Delta P_{\text{SRT}}^2 + B^2\Delta\Theta^2}, \quad (19)$$

where  $\Delta P_{\text{TRT}}$  is the uncertainty of a terrestrial telescope position adopted in the correlator,  $\Delta P_{\text{SRT}}$  is a displacement of the OD error of a satellite radio telescope,  $B$  is the projected baseline length to the celestial sphere at the source, and  $\Delta\Theta$  is the EOP error. Equation (19) can be expressed by the following approximation:

$$\sigma_{\phi_{\text{bl}}} [\text{deg}] \approx 13 \cdot \left( \frac{\nu [\text{GHz}]}{43 \text{ GHz}} \right) \left( \frac{\Delta\theta [\text{deg}]}{2^\circ} \right) \times \left[ \left( \frac{\Delta P_{\text{TRT}} [\text{cm}]}{1 \text{ cm}} \right)^2 + \left( \frac{\Delta P_{\text{SRT}} [\text{cm}]}{1 \text{ cm}} \right)^2 + 5.9 \cdot \left( \frac{B [\text{km}]}{25,000 \text{ km}} \right)^2 \left( \frac{\Delta\Theta [\text{mas}]}{0.2 \text{ mas}} \right)^2 \right]^{\frac{1}{2}}. \quad (20)$$

The residual phase errors with the typical parameters used in equation (20) are given in table 1.

<sup>2</sup> <<http://www.vlba.nrao.edu/memos/sci/>>.

### 3.4. Instrumental Phase Errors

In VLBI observations, instrumental phase errors are caused by changes in the electrical path lengths in transmitting cables, gravity deformation of antenna structures, depending on the observing elevation, and independent frequency standards controlling VLBI station clocks. Those phase errors usually show slow systematic drifts, depending on the ambient temperature and the observing elevation angles; it is difficult to predict this behavior from physical models with the accuracy required for the VLBI data analysis. Phase referencing observations with fast antenna switching for a closely located pair of sources can cancel almost all of the instrumental phase errors. In this report we do not consider the contributions of such phase errors.

### 3.5. Uncertainties in the Positions and Structures of Calibrators

If there is little information about the position and structure of the chosen phase referencing calibrator, fringe phase errors are induced in the phase compensation. The residual phase error,  $\sigma_{\phi_{\Delta s}}$ , due to the positional error of a calibrator,  $\Delta s^c$ , is approximated as

$$\sigma_{\phi_{\Delta s}} [\text{rad}] \approx \frac{\sqrt{2}\pi\nu\Delta\theta B\Delta s^c}{c}. \quad (21)$$

The positions of celestial objects are determined in the International Celestial Reference Frame (ICRF; Ma et al. 1998). The ICRF is defined by a set of extragalactic radio sources (ICRF sources) with simple and/or well-known structures (Ma et al. 1998; Fey et al. 2004). The ICRF sources have a typical astrometric accuracy of 0.3 mas at  $S$ -band (2.3 GHz) and  $X$ -band (8.4 GHz) based on the aggregation of geodetic and astrometric VLBI observations. Although the ICRF sources are well distributed over the sky, the sky coverage is not sufficient to provide suitable phase referencing calibrators. To make up for this, astrometric VLBI survey activities have progressed to find new phase referencing calibrators (Beasley et al. 2002). A typical astrometric accuracy of the new calibrator candidates is better than 5 mas (Petrov et al. 2006). The astrometric accuracy of those sources will be improved by repeated astrometric observations in the future. Equation (21) can be expressed with the following approximation:

$$\sigma_{\phi_{\Delta s}} [\text{deg}] \approx 46 \cdot \left( \frac{\nu [\text{GHz}]}{43 \text{ GHz}} \right) \left( \frac{\Delta\theta [\text{deg}]}{2^\circ} \right) \times \left( \frac{B [\text{km}]}{25,000 \text{ km}} \right) \left( \frac{\Delta s^c [\text{mas}]}{0.3 \text{ mas}} \right). \quad (22)$$

The residual phase errors with the typical parameters used in equation (22) are given in table 1.

There may be very few unresolved sources at space VLBI resolution. There is another possibility to use galactic water maser or silicon monoxide maser sources as phase referencing calibrators, but these galactic maser emissions may also be seriously resolved at VSOP-2 spatial resolution (Migenes et al. 1999). Because the contributions of source structures to the phase errors are dealt with case

**Table 1.** Residual phase errors of a space baseline for a 2° separate pair of sources.

Error item	RMS phase		
	8.4 GHz	22 GHz	43 GHz
$\sigma_{\phi_{\text{dtrp}}}$ *,†,‡	12°	31°	61°
$\sigma_{\phi_{\text{dion}}}$ *,†,§	4°	1°	1°
$\sigma_{\phi_{\text{strp}}}$ †,¶	15°	40°	78°
$\sigma_{\phi_{\text{sion}}}$ †,	25°	9°	5°
$\sigma_{\phi_{\text{bl}}}$ **,††	10°	27°	52°
$\sigma_{\phi_{\Delta s}}$ **,‡‡	9°	24°	46°

\* Switching cycle time of 60 s.

† Elevation angle of 45° at the ground surface.

‡ Typical tropospheric condition. ( $C_w = 2$ )

§ 50-percentile ionospheric condition. ( $C_i = 1.6 \times 10^{-5} \text{ TECU} \cdot \text{m}^{-5/6}$ )

¶ Tropospheric zenith excess path error of 3 cm.

|| VTEC error of 6 TECU.

\*\* Baseline length of 25000 km.

†† Antenna position error of 1 cm for a TRT, OD error of 3 cm for an SRT, and EOP error of 0.2 mas.

‡‡ Calibrator positional error of 0.3 mas.

by case, we do not discuss them in this report.

### 3.6. Thermal Noise

The phase error,  $\sigma_{\Delta\epsilon_{\text{therm}}}$ , due to thermal noise in phase referencing for a pair of VLBI telescopes is given by

$$\sigma_{\Delta\epsilon_{\text{therm}}} [\text{rad}] = \frac{\sqrt{2} k \overline{T_{\text{sys}}}}{\eta A_e \sqrt{\Delta\nu}} \sqrt{\frac{1}{S^t T^t} + \frac{1}{2S^c T^c}}, \quad (23)$$

where  $k$  is Boltzmann's constant,  $T_{\text{sys}}$  is the system noise temperature,  $A_e$  is the effective aperture,  $\eta$  is the coherence factor for the VLBI digital data processing, and  $\Delta\nu$  is the observing IF bandwidth;  $S^t$  and  $S^c$  are the flux densities of the target and calibrator, respectively;  $T^t$  and  $T^c$  are the scan durations of the target and calibrator, respectively. Bars over the parameters represent the geometric mean of two telescopes. The factor of 1/2 of  $1/(S^c T^c)$  comes from the interpolation process in which two neighboring calibrator scans are used for the phase compensation of a target scan between the two. Assuming two-bit sampling in analogue-to-digital (A/D) conversions and using a system equivalent flux density (SEFD), represented by  $2kT_{\text{sys}}/A_e$ , we obtain the following approximation:

$$\sigma_{\Delta\epsilon_{\text{therm}}} [\text{deg}] = 1.6 \times 10^{-5} \cdot \left( \frac{\Delta\nu [\text{MHz}]}{256 \text{ MHz}} \right)^{-\frac{1}{2}} \times \left[ \left( \frac{T^t [\text{s}]}{10 \text{ s}} \right)^{-1} \left( \frac{\overline{S_{\text{SEFD}}} [\text{Jy}]}{S^t [\text{Jy}]} \right)^2 + \left( \frac{2T^c [\text{s}]}{10 \text{ s}} \right)^{-1} \left( \frac{\overline{S_{\text{SEFD}}} [\text{Jy}]}{S^c [\text{Jy}]} \right)^2 \right]^{\frac{1}{2}}, \quad (24)$$

where  $\overline{S_{\text{SEFD}}}$  is the geometric mean of the SEFDs of two telescopes.

#### 4. Simulation Study for VSOP-2 Phase Referencing

There are some conflicting issues in phase referencing. For example, the geometrical and atmospheric systematic errors causing an image distortion can be reduced by selecting a closer calibrator. On the other hand, brighter calibrators are often preferable because the larger is the thermal noise in the calibrator fringe, the less successful will the phase connection be. If there are several calibrator candidates around a target, which is better for phase referencing, the closer, but fainter, or the brighter, but more distant? In the end, the important thing is to select the optimum combination at the observing frequency in order to make the residual phase errors as small as possible. Constraints on the separation angle or the switching cycle time for a single space baseline can be evaluated from the approximations described in the previous section. However, for the image synthesis with a large amount of  $(u, v)$  samples with multi-baselines, it is hard to predict the image quality from the approximations. In addition, cycle skips in the phase connection of the calibrator fringe phases, often occur as the observing frequency becomes higher, and/or as the switching cycle time becomes longer. Degradation in the image quality due to the cycle skips can hardly be predicted by an analytical method.

In order to verify the effectiveness of phase referencing with VSOP-2, we developed a simulation tool called ARIS (Astronomical Radio Interferometer Simulator). In this section we first introduce what and how VLBI errors are simulated. Demonstrations of VSOP-2 phase referencing observations performed with ARIS are also shown. We then focus on the imaging performance in VSOP-2 phase referencing under realistic conditions so as to determine the allowable observing parameters, such as the switching cycle time, the separation angle, the OD accuracy of the satellite, the tropospheric condition, and the calibrator flux density.

##### 4.1. Simulations of VLBI Fringe Errors with ARIS

###### 4.1.1. Atmospheric fringe phase errors

In ARIS the tropospheric phase fluctuations are modeled as a phase screen assuming Kolmogorov turbulence. This simple model is useful when considering the interferometric phase fluctuations due to the troposphere (Asaki et al. 1996). The grid interval of the screen is set to 1 m. Since, in ARIS, the inner and outer scales can be selected among  $2^p \times (\text{grid interval})$ , where  $p$  is a natural number, those scales are fixed to 1024 and 8192 m for the inner and outer scales, respectively. The phase screen is simulated for each terrestrial telescope site, and flows at a constant speed of  $10 \text{ m s}^{-1}$  along west wind. When one screen passes over the line-of-sight of a terrestrial telescope, another new one is created from the edge of the previous screen as a seed so as not to generate an unnatural gap between them. The altitude of the phase screen is 1 km, and the elevation dependence of the amplitude of the fluctuation is achieved by multiplying a factor of  $\sqrt{\sec Z_g}$  as shown in equation (10). A typical simulated time series

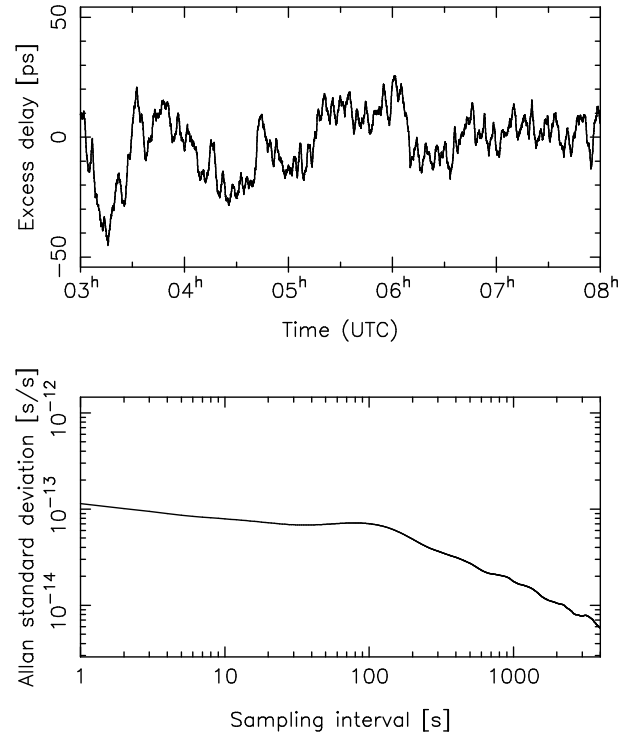


**Fig. 2.** Top: Typical simulated time series of the tropospheric excess path delay fluctuations of a space baseline under typical tropospheric conditions. The abscissa is time, and the ordinate is the excess path delay. The expectation is adjusted to 0 when the time series is generated. Bottom: Allan standard deviation calculated from the simulated time series shown at the top. The abscissa is the interval time, and the ordinate is the Allan standard deviation.

of the tropospheric fluctuations and the Allan standard deviation are shown in figure 2.

For ionospheric phase fluctuations, we consider two components in the TEC fluctuations: one is the MS-TID, and the other is a phase screen and assuming Kolmogorov turbulence driven by the MS-TID. The former is sinusoidal waves with a spatial wave length of 200 km and a propagating speed of  $100 \text{ m s}^{-1}$  at an altitude of 300 km. The latter has a grid interval of 150 m, and flows at the same speed and at the same altitude of the MS-TID. The inner scale of the screen is set to 76.8 km so as not to be over the spatial wave length of the MS-TID, and no transition region from the inner to outer scales of the SSF is provided in ARIS. Although there can be cases in which a single ionospheric phase screen covers separate terrestrial telescopes, the phase screen is independently simulated for each terrestrial telescope site.

The simulated MS-TID and phase screens are transmitted from the geographical poles to the equator along the longitudes. Recall that Kolmogorov turbulence is assumed to be driven by the MS-TID, so that the amplitude of Kolmogorov turbulence is proportional to that of the MS-TID. To determine the balance of the amplitudes between them, we analyzed short-term VTEC fluctuations, based on Noguchi et al. (2001), of TEC data taken with a

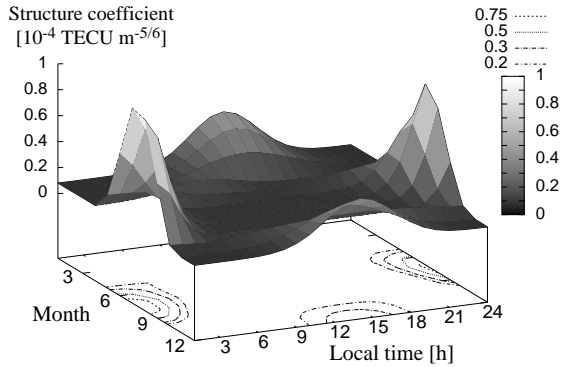


**Fig. 3.** Amplitude of the structure coefficient of the SSF of the TEC fluctuations versus local time and season for the northern hemisphere to be adopted in ARIS.

Japanese GPS receiver network operated by Geographical Survey Institute (GSI) of Japan (Saito et al. 1998). In this study we kept the balance so that  $C_i$  has its maximum value of  $10^{-4}$  TECU·m $^{-5/6}$  when the amplitude of the MS-TID is 1 TECU, the largest MS-TID amplitude often observed at mid-latitudes. Since the influence of the ionospheric phase fluctuations is generally smaller than that of the tropospheric phase fluctuations at the VSOP-2 observing frequency bands, we did not pay attention to various ionospheric conditions. Instead, the time evolution of the structure coefficient versus the local time and season for the northern hemisphere, as shown in figure 3, is given. This figure was obtained from an analysis based on Noguchi et al. (2001) with a smoothing process by means of an elliptical Gaussian fitting. From the GPS TEC analysis, the 50-percentile condition of  $C_i$  is  $1.6 \times 10^{-5}$  TECU m $^{-5/6}$ , as shown in figure 4. In ARIS, an unusual ionospheric status, such as a large-scale TID, plasma bubbles often observed at low-latitudes, and geomagnetic storms, is not considered. The elevation dependence of the amplitude of the fluctuations is achieved by multiplying a factor of  $\sqrt{\sec Z_i}$ . The simulated time series of the ionospheric fluctuations at 43 GHz, observed with a space baseline, and the Allan standard deviation are shown in figure 5.

The atmospheric systematic error was set randomly and independently for each terrestrial telescope in each simulation pass. The standard deviations were 3 cm and 6 TECU for the systematic errors of the zenith excess path length due to the water vapor and VTEC, respectively. The line-of-sight tropospheric excess path error is a product of the zenith path error and Niell's wet mapping function (Niell 1996). The line-of-sight TEC error is a product of the VTEC error and  $\sec Z_F$ . The altitude to calculate  $Z_F$  was set to 450 km.

#### 4.1.2. Geometrical phase errors and satellite trajectory in $(u, v)$

In ARIS a displacement in the a priori terrestrial telescope position adopted in the correlator is given as a dis-

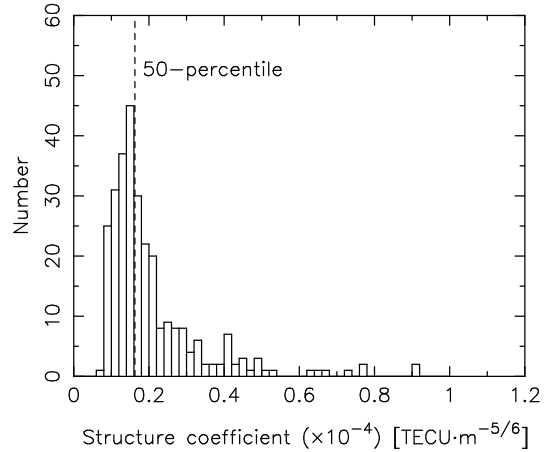


**Fig. 4.** Histogram of the structure coefficient of the SSF of the TEC fluctuations obtained from the GPS TEC data analysis. The data taken from 2001 January to December were analyzed with a method based on Noguchi et al. (2001). The vertical dotted line shows the 50-percentile condition.

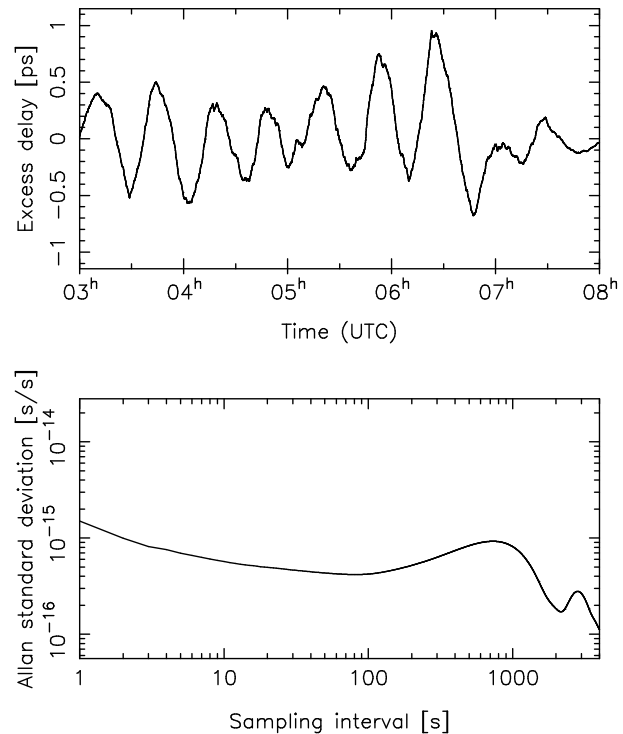


**Fig. 5.** Top: Typical simulated time series of the ionospheric excess path delay fluctuations of a space baseline in winter night time. The abscissa is time, and the ordinate is the excess path delay at 43 GHz. The expectation is adjusted to 0 when the time series is generated. Bottom: Allan standard deviation calculated from the simulated time series shown in the top. The abscissa is the interval time, and the ordinate is the Allan standard deviation in s/s.



placement vector. The standard deviations of the horizontal and vertical components are 3 mm and 1 cm, respectively, in the local tangent coordinates, and the displacement vector is set randomly and independently for each terrestrial telescope in each simulation pass. The EOP errors are given as offsets in the EOP transformation matrices defined by IERS Conventions (2003) (McCarthy, Petit 2004<sup>3</sup>). The offset of the celestial and terrestrial polar directions are randomly set with standard deviations of 0.3 mas, and the UT1 offset is randomly set with standard deviation of 0.02 ms. The systematic error of calibrator positions is given with the standard deviation of 0.3 mas, while the positional offset is logged in ARIS and used to estimate the astrometric accuracy of the target in the later analysis stage.

In ARIS the displacement vector of the satellite position is modeled in a co-moving frame: two unit vectors are aligned with the radial direction towards geocenter (radial component) and the orbital angular momentum vector (cross track component); the remained component is in the orbital plane (along track component) and orthogonal to the other two. The three components of the displacement vector are made from a combination of ad hoc trigonometric functions synchronizing with the true anomaly of the orbit. Since the OD accuracy would be the worst at apogee, as described in subsection 5.3, the root-square-sum (RSS) of the three components of the displacement at apogee is fixed to be four-times larger than that at perigee. The displacement vector is scaled up or down in order to investigate the influence of the OD error on the image quality. In the following discussion we use the OD displacement at the apogee (ODDA) as an indicator of the OD error. Figure 6 shows a trajectory of the satellite orbital motion and the OD displacement from the supposed trajectory in the case of the ODDA of 4 cm.

#### 4.1.3. How to generate corrupted fringes

The instantaneous complex visibility,  $\mathbf{V}(i, j, t, \nu_0)$ , for a baseline of telescopes  $i$  and  $j$  at time  $t$  and at the sky frequency at the IF band edge,  $\nu_0$ , is calculated from a two-dimensional Fourier transformation of a brightness distribution of a celestial source and the  $(u, v)$  trajectory every second. We assume that the delay difference and fast phase change due to the Earth rotation are largely removed in the correlator. The multi-channel frequency,  $\nu$ , in the IF bandwidth is  $\nu_0 + (m/M)\Delta\nu$ , where  $M$  is the number of the frequency channels, and  $m$  is 0, 1, 2, ...,  $M - 1$ . In ARIS the non-dispersive delay errors listed in table 1 (all but the ionospheric excess delay) are calculated for each telescope. Those delay errors are summed to obtain a total non-dispersive delay error,  $\tau_{\text{err1}}(i, t)$ . On the other hand the ionospheric delay error,  $\tau_{\text{err2}}(i, t, \nu)$ , for a terrestrial telescope is calculated with the line-of-sight TEC estimation error  $\Delta I$  by

$$\tau_{\text{err2}}(i, t, \nu) = -\frac{\kappa TEC_{\text{err}}}{c\nu^2}. \quad (25)$$

<sup>3</sup> IERS Conventions, No.32, ch5 (2004) is available at <<http://www.iers.org/iers/publications/tn/tn32/>>.

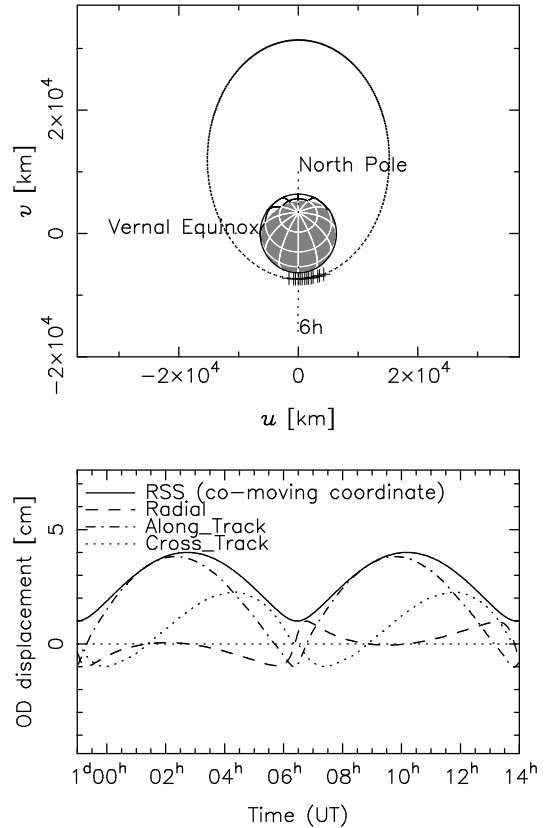


**Fig. 6.** Top: Simulated orbital trajectory of the VSOP-2 satellite projected to the  $(u, v)$  plane at  $(6^{\text{h}}, 59^{\circ})$ . Dots and crosses represent the trajectory out of and in the Earth shadow, respectively. The Earth size is represented by the central circle with the gray part of night. Bottom: Simulated OD displacement from the supposed trajectory of the satellite in the co-moving coordinates.

Then, the contribution of the delay errors to the antenna complex gain,  $\mathbf{G}(i, t, \nu)$ , is obtained by

$$\mathbf{G}(i, t, \nu) = \exp\{-j2\pi\nu[\tau_{\text{err1}}(i, t) + \tau_{\text{err2}}(i, t, \nu)]\}. \quad (26)$$

Thus, a fringe  $\mathbf{F}(i, j, t, \nu)$  of the source for the baseline is made by

$$\mathbf{F}(i, j, t, \nu) = \mathbf{G}(i, t, \nu)\mathbf{G}^*(j, t, \nu)\mathbf{V}(i, j, t, \nu_0), \quad (27)$$

where the asterisk represents complex conjugate, and  $\mathbf{V}$  is assumed not to vary with the frequency channels. A Gaussian noise vector, whose components correspond to the real and imaginary parts, is generated every second at each frequency channel for each baseline. Both components have an RMS amplitude of  $\frac{\overline{S_{\text{SEFD}}}(i, j, t, \nu_0)}{|\mathbf{V}(i, j, t, \nu_0)|} / (\eta\sqrt{2\Delta\nu/M})$ , where  $\overline{S_{\text{SEFD}}}(i, j, t, \nu_0)$  is the geometric mean of the SEFDs of the telescopes,  $i$  and  $j$  at the observing elevations at  $\nu_0$ , and assumed not to be varied with the frequency channels. The fringe including the thermal noise is generated by adding the noise vector. The parameters to simulate  $\tau_{\text{err1}}$  and  $\tau_{\text{err2}}$  are listed in table 2. Since the phase screen generation is the most time-consuming process in ARIS, the time-variation patterns of the atmospheric phase fluctuation

**Table 2.** Parameters used in the simulations.

Item	Type*	Quantity
$\Delta\theta$	V	0.5, 1, 2, 4, 8°
ODDA	V	2, 4, 8, 16, 32 cm
$\nu$	V	8.4, 22, 43 GHz
$C_w$	V	1, 2, 4
$v_w$ (west wind)	C	10 m s <sup>-1</sup>
$H_w$	C	1 km
$H_s$	C	1 km
$C_i$	...†	...†
$v_i$	C	100 m s <sup>-1</sup>
$H_i$	C	300 km
$\Delta l_z$	T	3 cm
$\Delta VTEC$	T	6 TECU
$H_F$	C	450 km
$\Delta P_{TRT}$ (vertical)	T	1 cm
(horizontal)	T	3 mm
Celestial pole offset	S	0.3 mas
Terrestrial pole offset	S	0.3 mas
UT1 offset	S	0.02 ms
$\Delta s^c$	S	0.3 mas

\* Type V items are interesting ones to verify the effectiveness of VSOP-2 phase referencing. Type C items have a constant value. Type T items are set for each telescope in each simulation pass among samples with the mean of 0 and the standard deviation given by “Quantity”. Type S items are set in each simulation pass among samples with the mean of 0 and the standard deviation given by “Quantity”.

† See subsection 4.1.1.

tuations are repeatedly used for various observing frequencies, ODDsA, and  $C_w$ .

#### 4.1.4. How to compensate for corrupted fringe phases

The phase-compensation process is performed in ARIS with a simple interpolation algorithm. The phase-compensated fringe phases are first vector-averaged for each scan. The calibration data,  $\Phi_{\text{cal}}$ , for the  $n$ -th target scan is

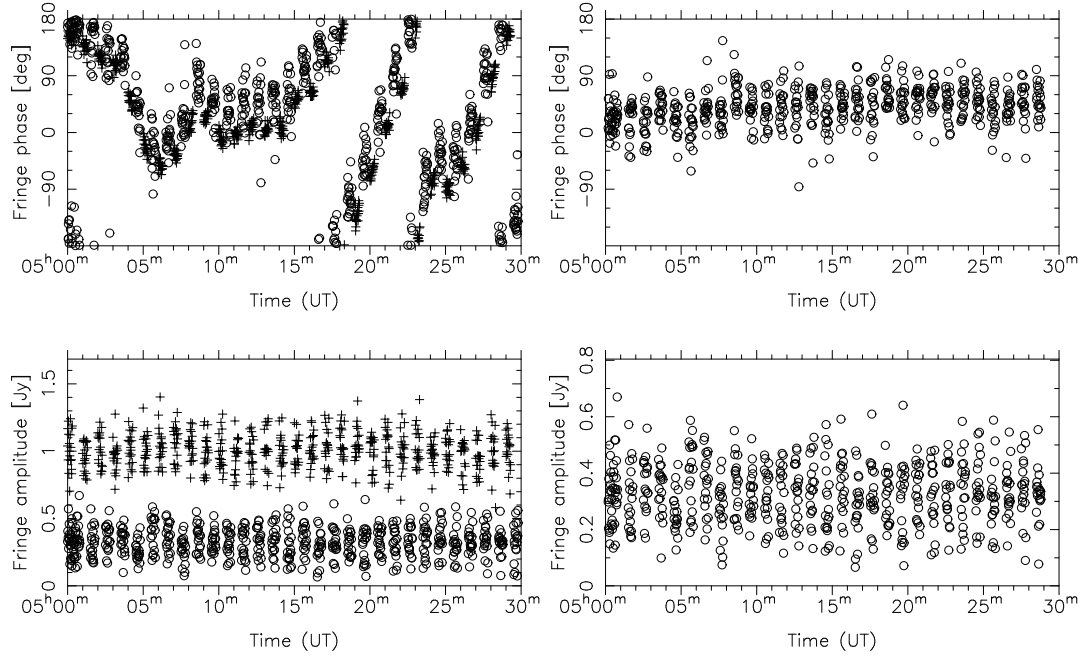
$$\Phi_{\text{cal}}(t) = \overline{\Phi}_n^c + \frac{(\overline{\Phi}_{n+1}^c - \overline{\Phi}_n^c + \Phi_{\text{adj}})(t - t_n^c)}{T_{\text{swt}}}, \quad (28)$$

where  $\overline{\Phi}_n^c$  is a vector-averaged calibrator fringe phase along the time and frequency followed by the  $n$ -th target scan,  $\overline{\Phi}_{n+1}^c$  is the following one, and  $t_n^c$  is the center time of the followed calibrator scan. An adjustment term,  $\Phi_{\text{adj}}$ , is selected among  $-2\pi$ , 0, and  $+2\pi$  radians to prevent  $|\overline{\Phi}_{n+1}^c - \overline{\Phi}_n^c|$  from being over  $\pi$  radians, so as not to induce a cycle skip between the neighboring calibrator scans. The compensated target fringe,  $\mathbf{F}^t(i, j, t, \nu)$ , is calculated from  $\mathbf{F}^t(i, j, t, \nu)$  and  $\Phi_{\text{cal}}(t)$  by

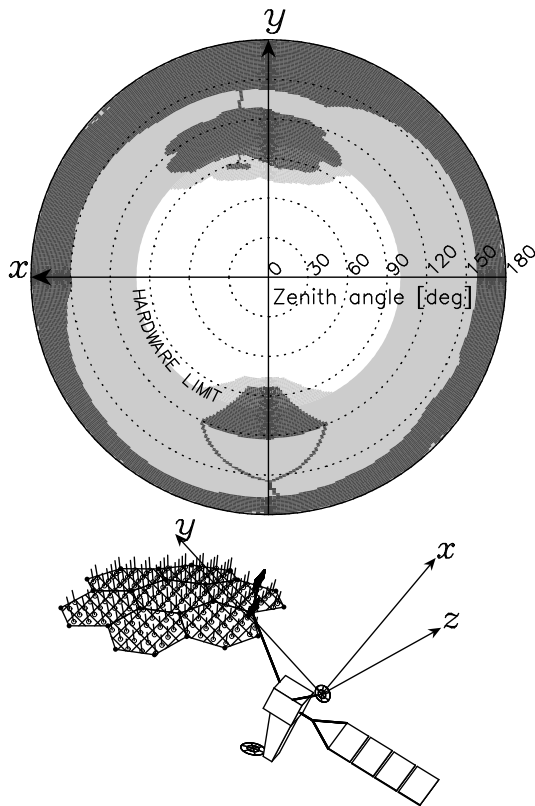
$$\mathbf{F}^t(i, j, t, \nu) = \mathbf{F}^t(i, j, t, \nu) \exp[-j\Phi_{\text{cal}}(t)]. \quad (29)$$

Figure 7 shows a demonstration of a phase referencing observation at 43 GHz, performed with ARIS, of a baseline consisting of the VSOP-2 satellite and a terrestrial telescope of the Very Long Baseline Array (VLBA) of National Radio Astronomy Observatory (NRAO) under good tropospheric conditions ( $C_w = 1$ ). The switching

cycle time and scan durations for both the target and calibrator are 60 and 20 seconds, respectively. Both are point sources, and the separation angle is 2°. The target and calibrator flux densities are 0.3 and 1 Jy, respectively. The ODDA is 4 cm. In this demonstration the coherence of the target fringe phase is improved by phase referencing from a situation including the prominent perturbations to an RMS phase of 30°.



**Fig. 7.** Simulated time series of the fringes of a VSOP-2 space baseline with a VLBA telescope at 43 GHz under good tropospheric conditions. The IF bandwidth is 256 MHz, the OD displacement at the apogee is 4 cm, the switching cycle time is 60 seconds, and the separation angle of the sources is  $2^\circ$ . The target and calibrator flux densities are 0.3 and 1 Jy, respectively. Left: Fringe phases (top) and amplitudes (bottom) of the target and calibrator. Open circles and crosses represent the target and calibrator fringes, respectively. Right: Fringe phase (top) and amplitude (bottom) of the target after phase referencing.



**Fig. 8.** Field of view of the data-link antenna based on the conceptual design of the satellite. The elevation limit of the data-link antenna is  $-10^\circ$  for the time being in this investigation. A light-gray region represents the masked area, because of the assumed elevation limit of the data-link antenna and satellite structure (dark gray region) in the near field.

#### 4.1.5. Observational limits on the satellite

The VSOP-2 observing time for phase referencing will be restricted by power-supply shortages of the satellite because of Earth eclipse, and inaccessible data-link because of the limited distribution of the ground tracking network and angular coverage of the on-board data-link antenna. In order to realistically simulate the  $(u, v)$  coverage with the space baselines, the following three conditions are considered: (1) phase referencing observations are suspended during partial and total Earth eclipses in the satellite orbit; (2) the ground tracking network used in VSOP (Hirabayashi et al. 2000) is assumed for VSOP-2; and (3) on-board link antenna coverage is tentatively generated from a blocking pattern based on the conceptual design of the satellite, as shown in figure 8.

#### 4.2. Allowable Separation Angle, Switching Cycle Time, and OD Error for VSOP-2 Phase Referencing

Because fast attitude switching of the VSOP-2 satellite for phase referencing will be achieved by actuator attitude control, we have to clarify the requirements of the control system in terms of the maneuvering speed and the angular range. The OD accuracy is also an issue to be discussed for the satellite system. Therefore, it is impor-

tant to clarify the allowable separation angle, switching cycle time, and OD error so as to determine the satellite design. Since the allowable switching cycle time is very dependent on the tropospheric condition and observing frequency, we must investigate the performance of phase referencing under various tropospheric conditions at each observing frequency. Here, we present a simulation series of VSOP-2 phase referencing observations for various separation angles, ODDsA, switching cycle times, tropospheric conditions, and observing frequencies.

##### 4.2.1. Simulation conditions

The simulation conditions are summarized in table 3. We simulated 15-hour observations with the VSOP-2 satellite and 10 VLBA telescopes. This observing time is almost double of the planned orbital period of the satellite. The lowest elevation angle for the terrestrial telescopes was set to  $20^\circ$ . The center position of pairs of sources was at  $(6^{\text{h}}, 59^\circ)$ . Such observing conditions were selected because (1) the highest spatial resolution in VSOP-2 is achievable; (2) long-term phase variations due to the geometrical and atmospheric systematic errors on the synthesized image can be tested; and (3) it is easy to investigate the influence of the sensitivity of the space baselines on the synthesized images by using a homogeneous terrestrial VLBI array. The SEFDs of the VLBA telescopes were taken from Napier (1995) as well as J. S. Ulvestad and J. M. Wrobel (2006, VLBA Observational Status Summary),<sup>4</sup> and are listed in table 4. Figure 9 shows an example of the  $(u, v)$  coverage of the simulations for the case of a  $2^\circ$  separate pair of sources. Although the variable ODDA with an expectation and distribution seems to be more realistic, much larger data sets will be needed to show the statistically reliable results in the current imaging simulations with only two orbits. To reduce the number of simulations in order to save the time, we adopted non-variable ODDsA of 2, 4, 8, 16, and 32 cm.

In ARIS, three tropospheric conditions of  $C_w = 1, 2,$  and  $4$ , that is, good, typical, and poor tropospheric conditions were examined. The time evolution of  $C_w$  during an observation is not considered, and an identical tropospheric condition is used for all of the terrestrial telescopes. To compare the results for various values of the interesting parameters, we did not change the observation season, or start time to switch the tropospheric condition, because the other conditions, such as the  $(u, v)$  coverage, should be identical throughout the simulations. The amplitude of the TEC disturbance varies along with the model, as shown in figure 3.

In the present simulations the target and calibrator were point sources with the flux densities of  $10^{-5}$  and  $10^{-4}$  of  $S_{\text{SEFD}}$ , respectively, of a space baseline with a VLBA telescope directed to the zenith, as listed in table 5. The flux densities of the target were 12, 14, and 23 mJy at 8.4, 22, and 43 GHz, respectively. While the VSOP-2 receivers have two IF bands each with 128 MHz in the conceptual design, the simulated observation system has,

<sup>4</sup> <<http://www.vlba.nrao.edu/astro/genuse/>>.

**Table 3.** Source positions, observing schedule, terrestrial telescopes, and orbital parameters.

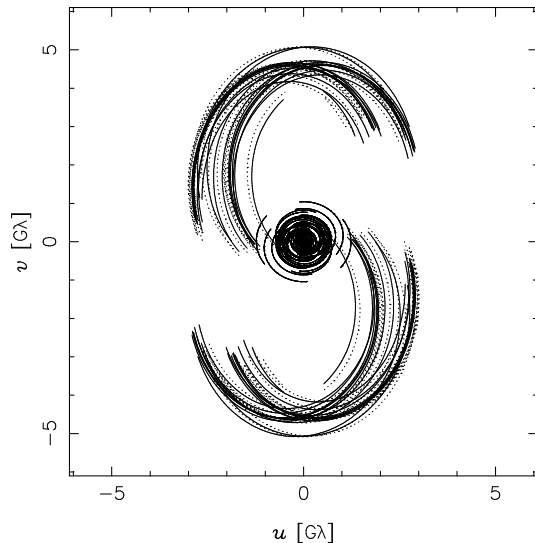
Center position of sources	RA(2000)=6 <sup>h</sup> 00 <sup>m</sup> 00 <sup>s</sup> Dec(2000)=59°00′00″
Observation start time	23h UT on Jan 1st
Observing time	15 hours
Terrestrial array	VLBA (10 telescopes)
Elevation limit of TRTs	20°
IF bandwidth	256 MHz
A/D quantization level	Two-bit sampling
Output IF band	1
Output frequency channel	1
Inclination	31°
RA of the ascending node	180°
Argument of perigee	−90°
Apogee height	25000 km
Perigee height	1000 km
Time of perigee passage	Observation start time

**Table 4.** SEFDs of the VSOP-2 SRT and the VLBA telescopes.

Telescope	Frequency	SEFD
SRT	8.4 GHz	4708 Jy
	22 GHz	2353 Jy
	43 GHz	3766 Jy
VLBA*	8.4 GHz	307 Jy <sup>†</sup>
	22 GHz	888 Jy <sup>†</sup>
	43 GHz	1437 Jy <sup>†</sup>

\* Napier (1995); J. S. Ulvestad and J. M. Wrobel (2006).

† Estimate to the zenith direction.

**Fig. 9.** Example of  $(u, v)$  coverage of a VSOP-2 observation at 43 GHz for a 2° separate pair of sources along with Right Ascension. The terrestrial array is 10 VLBA telescopes. Solid and dashed lines represent the target and calibrator, respectively.**Table 5.** Flux densities of the target and calibrator in the first simulation series.

Item	8.4 GHz	22 GHz	43 GHz
$\overline{S_{\text{SEFD}}^*}$	1202 Jy	1445 Jy	2326 Jy
$S^t$ ( $\overline{S_{\text{SEFD}}} \times 10^{-5}$ )	12 mJy	14 mJy	23 mJy
$S^c$ ( $\overline{S_{\text{SEFD}}} \times 10^{-4}$ )	120 mJy	145 mJy	233 mJy

\* Geometric mean of SEFDs of the SRT and a VLBA antenna to the zenith.

for simplicity, a single frequency channel with a bandwidth of 256 MHz. Although a coherence loss of about 10% for the 256-MHz bandwidth occurs if a group delay error of 1 ns exists, the amplitude degradation was not considered in the present study. An independent phase drift in each IF band, which may cause a problem in their combination, was also not considered.

We conducted two cases for switching cycle times of 60 and 40 seconds. In the simulations, the slew time of all the telescopes was fixed to 10 seconds when changing the pointing for all the separation angles, so that the scan durations were 20 and 10 seconds for switching cycle times of 60 and 40 seconds, respectively. The expected signal-to-noise ratios for a single calibrator scan of 20 and 10 seconds are 8.6 and 6.0, respectively, for the space baselines with assumptions of a bandwidth of 256 MHz, two-bit sampling in the A/D conversion, and the terrestrial telescope directed to the zenith.

Baseline-based phase referencing were carried out in ARIS. The phase-compensated target fringes were stored in the FITS-IDI format to load into the NRAO Astronomical Image Processing System (AIPS). Phase-compensated fringes were Fourier inverted and deconvolved (CLEANed) with AIPS IMAGR to obtain synthesized images. A typical beam size at 43 GHz with uniform weighting was 80 and 38  $\mu\text{s}$  for the major and minor axes, respectively, with a position angle of 86°. At 8.4 and 22 GHz the beam size increased by factors of 5.1 and 2.0, respectively. We set the image pixel size to 19, 7, and 3.8  $\mu\text{s}$  at 8.4, 22, and 43 GHz, respectively. The synthesized image size was fixed to 256  $\times$  256 pixels centered at the phase tracking center. A CLEAN box centered on the imaged area has a 100  $\times$  100-pixel size. Here, we call the CLEAN image with the phase-compensated data a phase referencing direct image.

Since the calibrator position was set with the randomly generated positional offset, the brightness distribution of the phase referencing direct image was shifted from the phase tracking center almost as much as the positional offset of the calibrator logged by ARIS. This positional shift from the origin is used to estimate the relative position of the target to the calibrator. If the imaged area is not wide enough to follow the positional shift by chance, the brightness distribution may go outside of the area. In the current simulations, plenty of data sets were processed, so that the iteration process with step-by-step inspections should be excluded to save time. Therefore, the phase tracking center of the compen-

sated target data was automatically corrected with AIPS UVFIX by the coordinate rotation with the rotation axis  $\mathbf{e} = [(\mathbf{s}^c + \mathbf{s}^t) \times (\mathbf{s}^c - \mathbf{s}'^c)] / |(\mathbf{s}^c + \mathbf{s}^t) \times (\mathbf{s}^c - \mathbf{s}'^c)|$  and rotated angle  $\Psi = 2 \arcsin \left[ |\mathbf{s}^c - \mathbf{s}'^c| / 2\sqrt{1 - (\mathbf{s}^c \cdot \mathbf{e})^2} \right]$ , where  $\mathbf{s}^t$  and  $\mathbf{s}^c$  are unit vectors pointing to the target and calibrator, respectively, and  $\mathbf{s}'^c$  represents the calibrator position adopted in the correlator.

Independent simulations with the same values of  $C_w$ , ODDA, and separation angle were carried out for 16 pairs of sources with 16 different position angles spaced at  $22^\circ.5$  intervals. The surface brightness peak value and its positional offset from the corrected phase tracking center were obtained in each image. Those results were averaged over the 16 different positions for statistical reliability.

We used the ratio of the averaged brightness peak value to the model as an indicator to evaluate the resultant image quality without any dependence on the thermal noise of the target and  $(u, v)$  coverage. We refer to the ratio as ‘‘image coherence.’’ The averaged positional offset was used as an indicator of astrometric accuracy of the phase referencing direct images.

#### 4.2.2. Results

The loss of the image coherence for the 60-s switching cycle is shown in figure 10 for the various separation angles and ODDsA. In general, the image coherence loss increases as the observing frequency and/or the tropospheric phase fluctuations increase because it becomes more difficult to correctly connect calibrator fringe phases between the scans. The image coherence loss also increases as the separation angle and/or ODDA increase because residual long-term phase variations distort the synthesized images. According to Thompson, Moran, Swenson (2001), temporally averaged visibility degrades as  $e^{-\sigma_\phi^2/2}$  where  $\sigma_\phi^2$  is the variance of a random Gaussian phase noise. In this report we tentatively put a threshold criterion of successful phase referencing onto the image coherence of 61% ( $e^{-\sigma_\phi^2/2} \simeq 0.61$  when  $\sigma_\phi = 1$  radian); in other words, image coherence loss of 39%. At 8.4 GHz, phase referencing is promising for all the tropospheric conditions, even with the ODDA of a few tens of centimeters. The simulation results indicate that the separation angle is recommended to be smaller than  $4^\circ - 5^\circ$ . At 22 GHz the separation angle is recommended to be smaller than  $1^\circ$  under poor tropospheric conditions, while phase referencing can be useful for a separation angle within  $2^\circ - 3^\circ$  under good and typical tropospheric conditions. There is little difference in the image coherence loss at 22 GHz between the good and typical tropospheric conditions. This indicates that the 60-s switching cycle is short enough to cancel the short-term phase fluctuations at 22 GHz under typical tropospheric conditions, or better, but not enough under poor tropospheric condition. At 43 GHz it is not recommended that the phase referencing observations are conducted under poor tropospheric condition because serious coherence loss is caused by tropospheric phase fluctuations. Under typical tropospheric conditions, phase referencing can be useful if the separation angle is smaller than  $1^\circ$ . Under good tropospheric conditions, the separa-

tion angle is recommended to be smaller than  $1^\circ - 2^\circ$ .

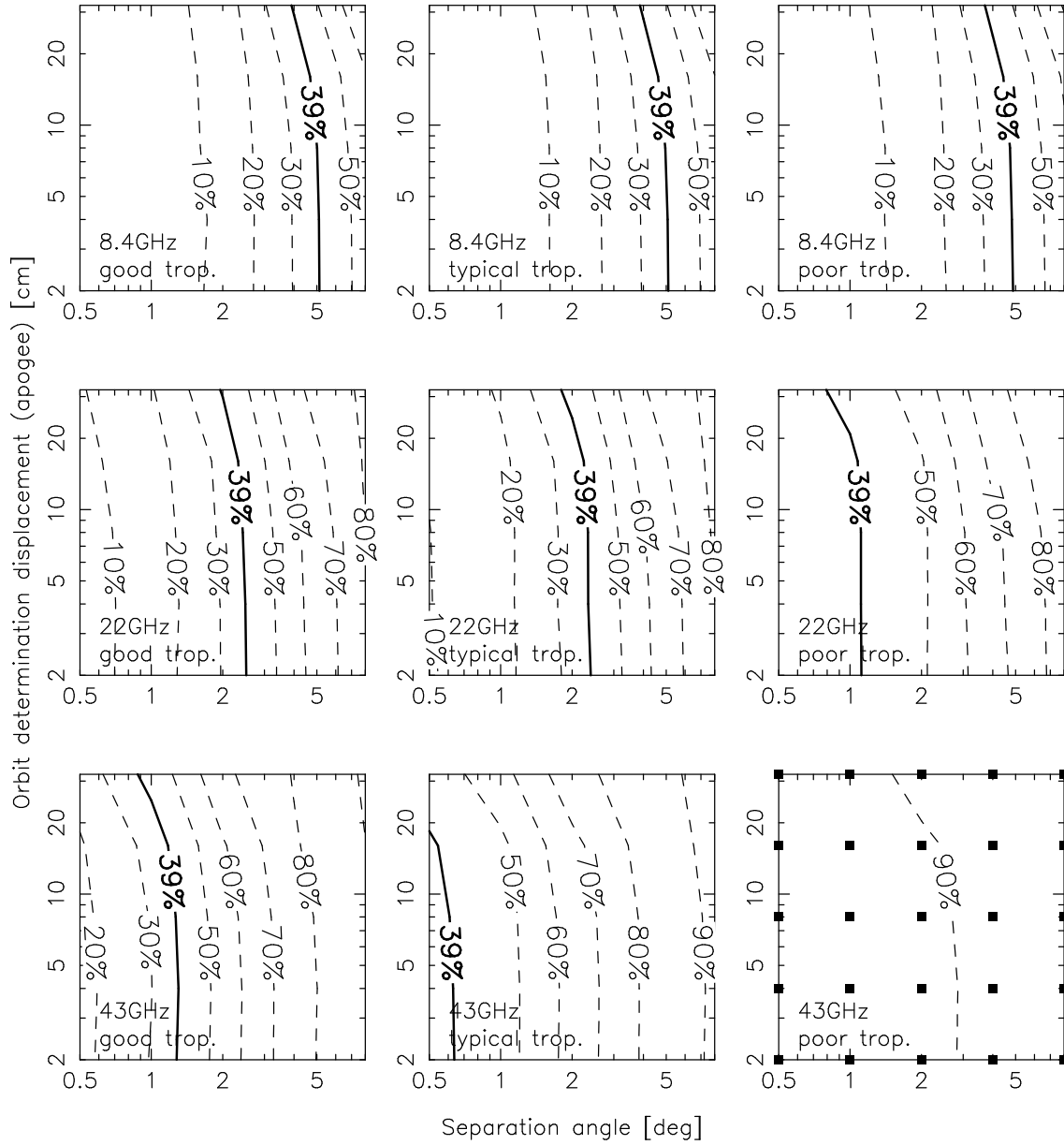


**Fig. 10.** Image coherence loss of the VSOP-2 phase referencing direct image with all the baselines in the case of the 60-s switching cycle. The abscissa and ordinate are the separation angle and OD displacement at the apogee in log scale, respectively. The contours show the percentage of the degradation relative to the model flux density of the target (10, 20, 30, 39, 50, 60, 70, 80, 90%). The top, middle, and bottom rows show the cases of 8.4-, 22-, and 43-GHz simulations. There are three plots in each row showing the good, typical, and poor tropospheric conditions. The filled squares in the right-bottom plot represent simulated grid.

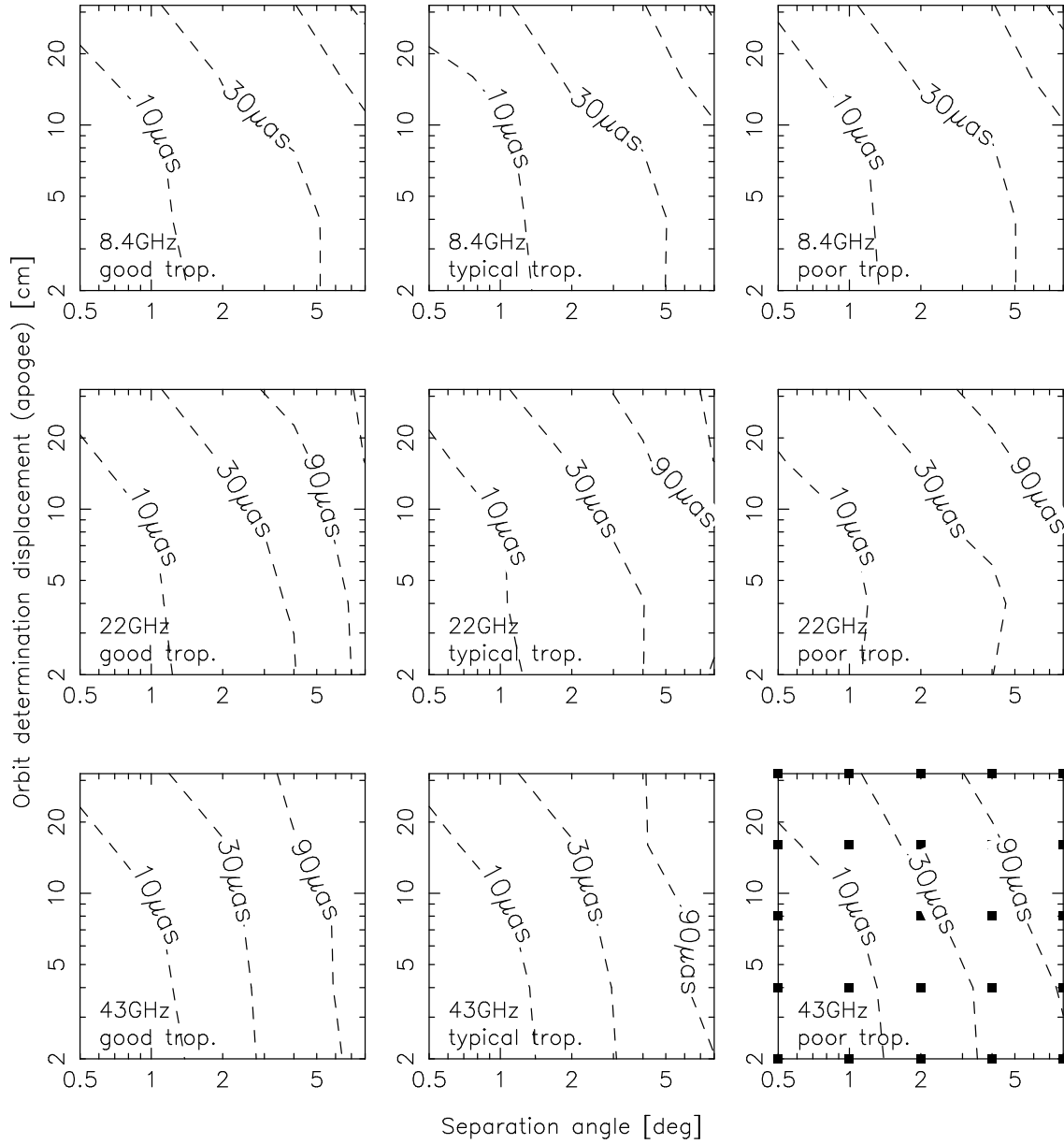


**Fig. 11.** Astrometric accuracy of the VSOP-2 phase referencing direct image with all the baselines in the case of the 60-sec switching cycle. The contours show the positional offset of the image peak from the phase tracking center (10, 30, 90, 190  $\mu$ s). The abscissa and ordinate are the separation angle and the OD displacement at the apogee in log scale, respectively. The top, middle, and bottom rows show the cases of 8.4-, 22-, and 43-GHz simulations. There are three plots in each row showing the good, typical, and poor tropospheric conditions. The filled squares in the right bottom plot represent simulated grid.



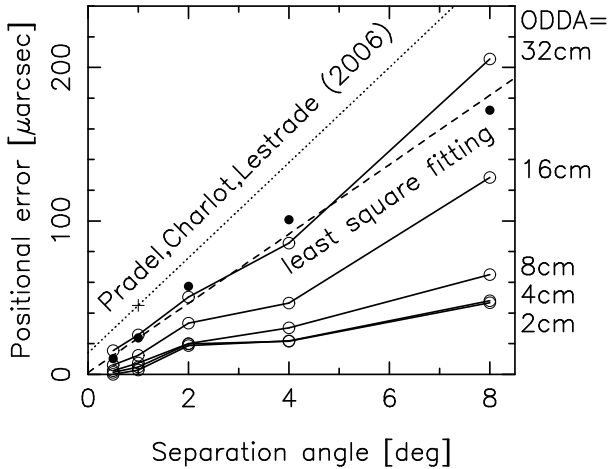


**Fig. 12.** Astrometric accuracy of the surface brightness peak of the phase referencing direct image of the VLBA and VSOP-2. The abscissa is the separation angle, and the ordinate is the positional offset. Filled circles and the dashed line represent simulation results for the VLBA and the least square fitted line, respectively. Open circles represent VSOP-2 simulation results. The astrometric accuracy for the VLBA obtained with SPRINT software described by Pradel, Charlot, Lestrade (2006) is also shown by the cross mark and the dotted line with an assumption of their empirical formula.

The astrometric accuracy for the 60-s switching cycle are shown in figure 11 for various separation angles and ODDsA. Phase referencing with VSOP-2 gives us an astrometric accuracy of better than  $30 \mu\text{as}$ , in general, if the phase referencing direct image can be obtained without any serious image coherence loss. There are no prominent differences in the positional offset between the different tropospheric conditions as well as the different observing frequency bands. This is because the astrometric accuracy is directly related to the geometrical delay measurement accuracy. All of the VLBI delay errors, except for the ionospheric one, are non-dispersive for the observing frequency, and the ionospheric delay error is not serious at the VSOP-2 observing frequency bands. Because the tendency about the astrometric accuracy is common for all of the simulation results in this study, we do not show the astrometric accuracy for the other cases mentioned below.

At this stage let us consider possible advantages of VSOP-2 phase referencing from the viewpoint of astrometry compared with terrestrial VLBI arrays. We carried out ARIS simulations of VLBA phase referencing observations for a comparison. We adopted the same parameters as given in tables 2 to 5 for VLBA simulations, and the tropospheric condition was typical. The comparison described below was made at 8.4 GHz. In addition to the ARIS simulations, SPRINT software described by Pradel, Charlot, Lestrade (2006) (hereafter, PCL2006) was also used for VLBA simulations for  $1^\circ$  pairs of sources with the center position at a declination of  $59^\circ$  in order to check the behavior of ARIS. We carried out SPRINT simulations for 16 pairs of sources with the different position angles spaced equally. The phase referencing astrometric accu-

racy for a separation of  $1^\circ$ ,  $\Delta_{\alpha\cos\delta,\delta}^{1^\circ}$ , defined by PCL2006, was obtained by averaging all of the pairs. Note that several of the parameters and conditions in the SPRINT simulations are different from those in ARIS: for example, the switching cycle time was 150 seconds, the lower elevation limit was  $7^\circ$ , the flux densities of both the target and the calibrator were 1 Jy, and not the ionospheric error, but the static component of the dry tropospheric error was considered. It should also be noted that the calibrator positional accuracy of  $0.3 \text{ mas}$  was set in SPRINT. Simulation results of the astrometric accuracy are shown in figure 12 together with the simulation results of VSOP-2 phase referencing for the typical tropospheric condition, as already shown in figure 11. Assuming the empirical formula established by PCL2006 and the resultant  $\Delta_{\alpha\cos\delta,\delta}^{1^\circ}$  of  $45 \mu\text{as}$  from the SPRINT simulations, the ARIS results show systematically better performance than SPRINT. We carried out ARIS simulations for the case of the 150-s switching cycle; no distinguishable change could be seen from the 60-s switching cycle case. We then tested additional SPRINT simulations with an elevation limit of  $20^\circ$  for a pair of sources separated along with the declination, and obtained  $\Delta_{\alpha\cos\delta,\delta}^{1^\circ}$  of  $38 \mu\text{as}$ , which is much more consistent with the ARIS simulation results. We consider that the discrepancy in the results between the two simulators might be attributed to the different elevation limit, and that this discrepancy can be much smaller if the simulation parameters are adjusted to match each other. We then compared the astrometric accuracy of the VLBA with VSOP-2. When the ODDA is less than several centimeters, the astrometric accuracy of VSOP-2 is much superior to that of the VLBA. PCL2006 indicated that the global VLBI array, which is the combination of the VLBA and European VLBI network, cannot improve the astrometric accuracy very much compared with the VLBA. In general, because the telescopes in the global VLBI array observe sources at low elevations for the longest baselines, the atmospheric systematic error must be more severe in those baselines. Since much longer baselines are available in VSOP-2 without serious atmospheric phase errors, VSOP-2 phase referencing has an advantage compared with terrestrial VLBI arrays, unless the fringes of the space baselines are affected by the systematic phase error related to the OD. Assuming the tropospheric zenith error of 3 cm and the elevation limit of  $20^\circ$ , the allowable ODDA to achieve a higher astrometric accuracy with VSOP-2 can be roughly estimated at  $3 \times 3 \text{ cm} / \sin 20^\circ \sim 26 \text{ cm}$ , where the factor of three comes from the ratio between the maximum space and the terrestrial baseline lengths. From the simulation results, in cases where the ODDA is smaller than the 30-cm level, the astrometric accuracy of VSOP-2 is superior to the terrestrial VLBI arrays, as shown in figure 12.

For shorter switching cycle times, the image coherence can be improved for worse tropospheric conditions at the higher observing frequency bands. Figure 13 shows the image coherence loss for the 40-s switching cycle under the typical tropospheric condition. At 43 GHz an improvement can clearly be seen in the 40-s switching cycle, while there is little difference between the switching cycle

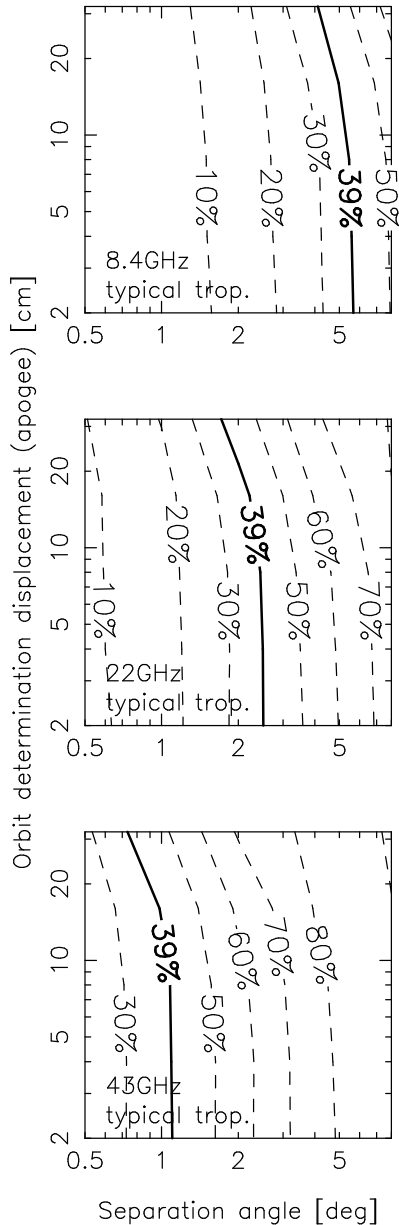


**Fig. 13.** Same as figure 10 for the typical tropospheric condition, but the switching cycle time of 40 seconds.

cle times of 60 and 40 seconds at 8.4 and 22 GHz. We also conducted simulations for the 40-s switching cycle under good tropospheric conditions, and there was little improvement in all of the observing frequency bands. On the other hand, simulations at 22 GHz under poor tropospheric conditions showed an improvement, and the allowable separation angle was stretched to  $2^\circ$ . At 43 GHz it is not recommended that the phase referencing observations are conducted under poor tropospheric conditions, even with the 40-s switching cycle.

The image coherence loss seems to be insensitive to the ODDA. This may be because there are only ten space baselines among 55 baselines in the simulations. To investigate the influence of the ODDA on the image coherence,

the phase referencing direct images were made only with 10 space baselines. The image coherence loss for the typical tropospheric condition and 60-s switching cycle time is shown in figure 14. The results show that the image coherence loss is more sensitive to the ODDA than that with all of the baselines, and is almost insensitive to an ODDA smaller than  $\sim 10$  cm. This indicates that the 10-cm level ODDA meets VSOP-2 phase referencing. We note that the image coherence in figure 14 is better compared with that in figure 10. This is because the fringe phase of the space baseline includes a single atmospheric phase error, while that of the terrestrial baseline includes a double one, so that the latter is less stable than the former, especially for small ODDsA. This does not mean, however, that the phase referencing direct image only with the space baselines is superior to the image with all of the baselines, because the image RMS noise of the former is worse than the latter.

The above recommendations may be too strict in some important applications. For example, the fringe at 43 GHz was subject to a serious coherence loss under poor tropospheric conditions, but an isolated peak could be seen in simulated images at the expected target position if the separation angle was rather less than  $1^\circ$ . Although the amplitude degradation cannot be recovered with the following self-calibration because the time scales of the residual phase fluctuations are typically shorter than a few minutes, the amplitude can be corrected by multiplying a factor of  $e^{\sigma_\phi^2/2}$  for the baseline, where  $\sigma_\phi$  is the RMS phase. Thus just for the astrometry, observers are less worried about the tropospheric conditions than those who are interested in the target morphology.

In general, the simulation results show that the image coherence is insensitive to an ODDA smaller than  $\sim 10$  cm. However, we obtained another indication of whether the atmospheric systematic errors were not included in the simulations. Figure 15 shows the case with no atmospheric systematic errors under the typical tropospheric condition for the 60-s switching cycle phase referencing with all of the baselines. The performance was greatly improved comparing with the cases involving atmospheric systematic errors. In addition, the smaller the ODDA, the wider can the allowable separation angle be. Reid, Readhead, Vermulen, Treuhaft (1999) showed that the atmospheric systematic errors should be calibrated for very precise astrometric VLBI observations at 43 GHz. They used a pair of sources to calibrate the atmospheric zenith delay errors by measuring the phase difference between them. Two phase referencing calibrators, or more, would be needed for the terrestrial array to calibrate the atmospheric systematic errors towards the best performance of VSOP-2 phase referencing.

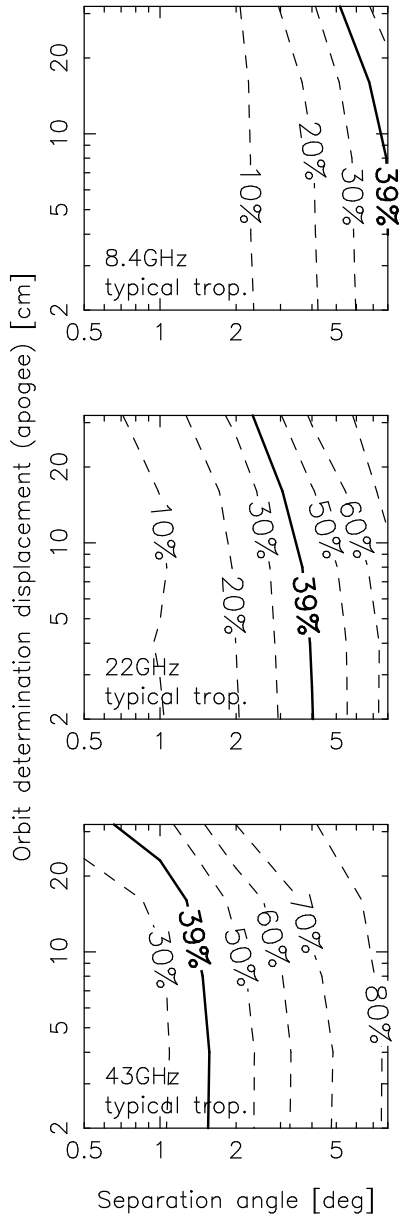


**Fig. 14.** Same as figure 10 for the typical tropospheric condition, but the phase referencing direct images are made only with the space baselines.

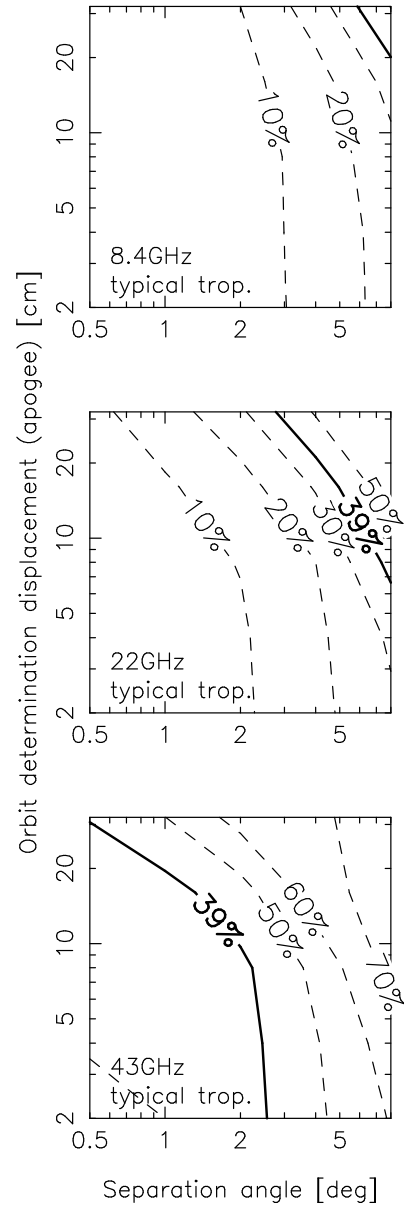


**Fig. 15.** Same as figure 10 for the typical tropospheric condition, but with no atmospheric systematic errors.

### 4.3. Allowable Calibrator Flux Densities

It is plausible that the effectiveness of phase referencing decreases with fainter calibrators, because the fainter the calibrator, the more difficult will be the phase connection, due to thermal noise. We carried out another simulation series by varying the calibrator flux density from  $10^{-5}$  to  $10^{-4}$  of  $\overline{S}_{\text{SEFD}}$  of a space baseline with a separation angle of  $1^\circ$  and an ODDA of 4 cm. In this simulation series, the calibrator flux densities ranged over 12–120, 14–145, and 23–233 mJy at 8.4, 22, and 43 GHz, respectively, and the target flux densities were the same as listed in table 5.

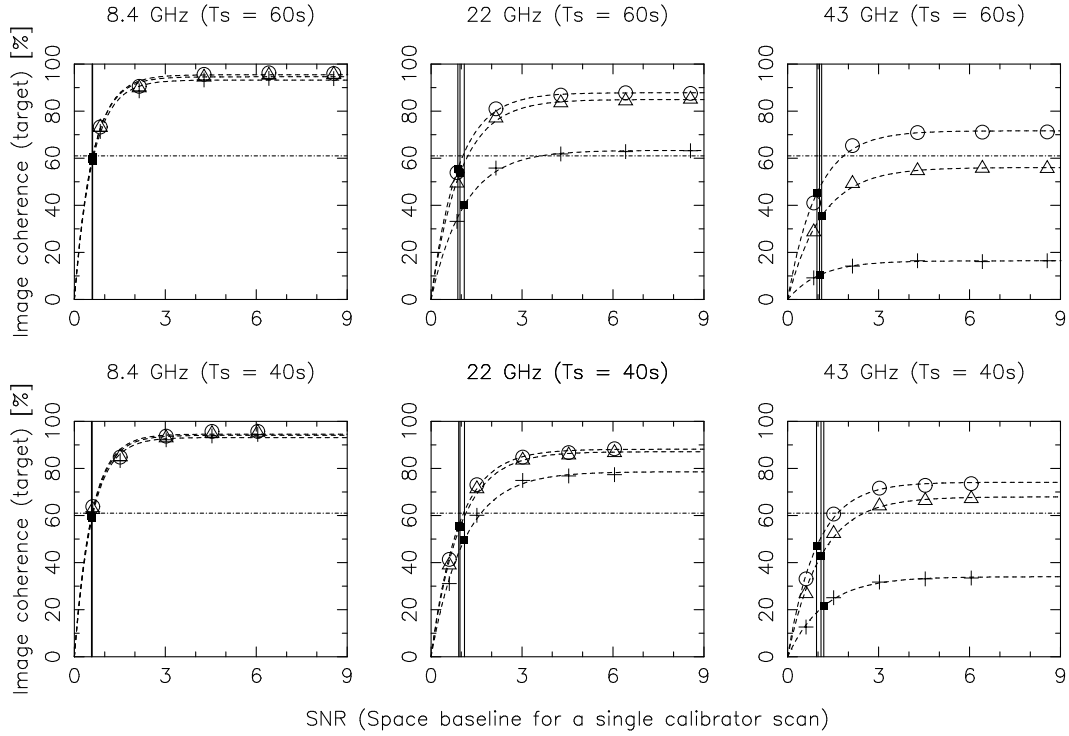
Figure 16 shows the image coherence obtained with all of the baselines as a function of the signal-to-noise ratio of a space baseline for a single calibrator scan. The image coherence drops as the calibrator flux density or the signal-to-noise ratio becomes smaller. The image coherence,  $Q$ , under the same tropospheric condition at the same observing frequency band can be well fitted to  $Q = Q_0(1 - e^{-\xi \cdot \text{SNR}^c})$ , where  $Q_0$  and  $\xi$  are the fitting parameters, and  $\text{SNR}^c$  is the signal-to-noise ratio of a space baseline for a single calibrator scan, represented by  $\eta(S^c / \overline{S}_{\text{SEFD}}) \sqrt{2\Delta\nu T^c}$ . It is noted from figure 16 that the fitted curve shapes at 22 and 43 GHz resemble each other, while those at 8.4 GHz differ. This is because the ratios of  $\overline{S}_{\text{SEFD}}$  between the space and terrestrial baselines at 22 and 43 GHz are 2.2, by chance, while the ratio at 8.4 GHz is 15.3. Therefore, the image qualities at 8.4 GHz are more supported by the sensitivity of the terrestrial baselines than those at 22 and 43 GHz.

Figure 17 shows the simulation results of the image coherence with only the space baselines. It is noted that  $\xi$  ranges over 1.1–1.4 under all the tropospheric conditions at all observing frequency bands. We carried out simulations with two other parameter combinations of the separation angle and ODDA ( $2^\circ$  separation and 4-cm ODDA, and  $1^\circ$  separation and 8-cm ODDA), and found that there is no prominent difference in  $\xi$  for the various parameter combinations. From simulations with only the space baselines,  $\xi$  seems to be uniquely determined by the sensitivity of baselines, while  $Q_0$  is dependent on the observing frequency, tropospheric condition, switching cycle time, separation angle, and ODDA.

The image coherence loss due to thermal noise is kept below 2–4% for an  $\text{SNR}^c$  of 4. Since the least sensitive baselines will be the space baselines in VSOP-2, it is safe for successful phase connection to choose calibrators with an  $\text{SNR}^c$  larger than 4. An  $\text{SNR}^c$  of 4, however, may lead to a false fringe detection in the fringe fitting for the calibrator. For good and typical tropospheric conditions, the coherence time at 22 and 43 GHz can be extended to be a few minutes, so that a possible solution to avoid false detection is to set the averaging time in the fringe fitting to a time interval including two to three calibrator scans.

Another possible way is to make frequent fringe-finder scans interleaved in a nominal phase referencing observation: because a fringe-finder, such as an ICRF source, is bright and has a well-known position, fringe-finder scans

are used to check the observing system and to calibrate the clock synchronization errors in VLBI observations. If the delay synchronization errors can be calibrated by group delay solutions with an accuracy of 1 ns, phase-slope in the single IF bandwidth of 128 MHz will cause only a 3% coherence loss. This might lead to the conclusion that the phase referencing calibrators can be used without any fringe fitting before phase referencing, and that we may use the calibrators with an  $\text{SNR}^c$  of 4. To observe the fringe-finders frequently, a high-speed maneuvering capability for rather larger separation angles compared to the switching maneuvering will be needed.



**Fig. 16.** Image coherence of the VSOP-2 phase referencing direct image with all the baselines as a function of signal-to-noise ratio of a space baseline for a single calibrator scan,  $SNR^c$ . The top and bottom rows show the cases of 60-s and 40-s switching cycle times, respectively. All the simulation has the condition of  $1^\circ$  separate pairs of sources and 4-cm ODDA. The calibrator flux densities in the simulations correspond to 10, 25, 50, 75, and 100% of  $10^{-4}$  of the geometric mean of SEFDs of the SRT and a VLBA telescope. The open circles, triangles, and crosses represent the good, typical, and poor tropospheric conditions, respectively. Horizontal dotted lines represent the crossed position to the threshold (39% image coherence loss). The dashed lines are fitted curves to  $Q_0(1 - e^{-\xi \cdot SNR^c})$  for each tropospheric condition. The filled squares and vertical lines represent the positions where  $\xi \cdot SNR^c = 1$ .

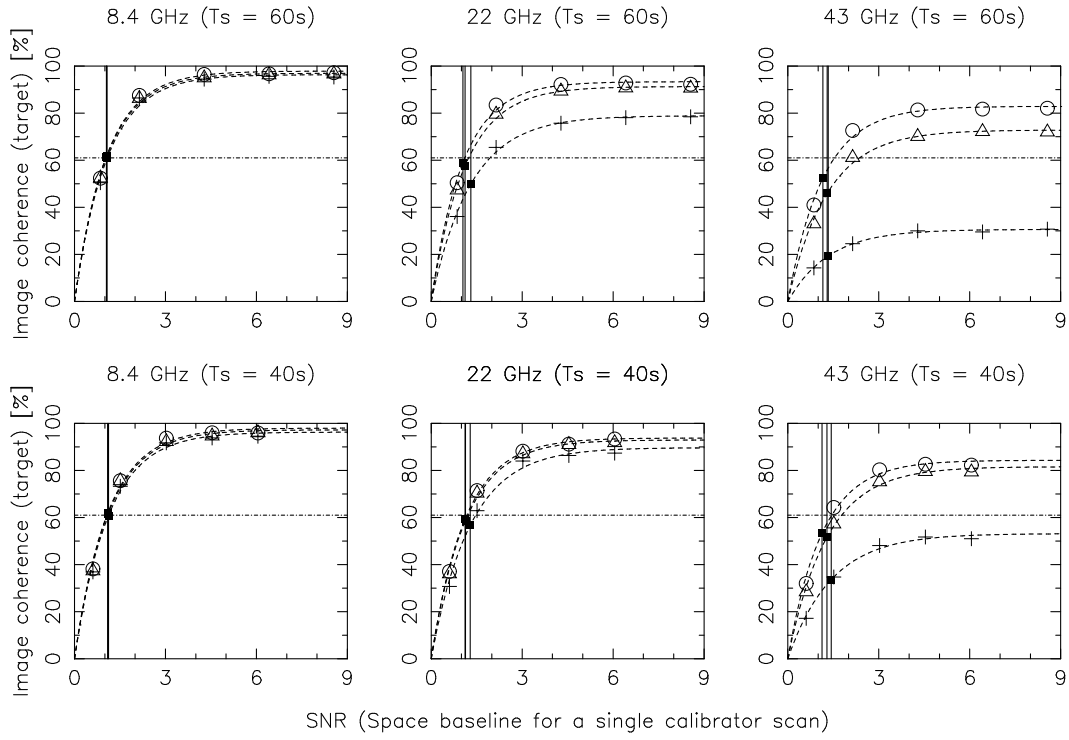


Fig. 17. Same as figure 16, but only with the space baselines.

## 5. Discussion

### 5.1. Calibrator Source Counts

In the previous section we obtained constraints on the calibrator flux densities for the successful phase referencing with VSOP-2. For the VLBA as a terrestrial array, calibrators are recommended to have flux densities larger than 56, 68, and 109 mJy at 8.4, 22, and 43 GHz, respectively, in the case of a 20-s calibrator scan, and 79, 96, and 154 mJy, respectively, in the case of a 10-s calibrator scan. Here we made use of two VLBI survey catalogues at *S*-band and *X*-band to investigate the probability to find a suitable calibrator located closely to an arbitrary target. The first is the VLBA calibrator catalogue, which can be accessed on-line<sup>6</sup>. This catalogue contains 3357 sources based on the VLBA Calibrator Survey (VCS) (Beasley et al. 2002; Fomalont et al. 2003; Petrov et al. 2005; Petrov et al. 2006). The ICRF sources are included in the catalogue as well. We can refer positions, integrated map flux densities, and unresolved map flux densities of compact sources observed with the VLBA, whose longest baseline is nearly 8000 km. The second is the Goddard Space Flight Center (GSFC) astrometric and geodetic catalogue, “2005f astro catalogue of compact radio sources (2005f\_astro)”<sup>7</sup>. This catalogue provides calibrated visibility FITS-IDI data on the web as well as an html version of the source list. The catalogue 2005f\_astro contains 3481 objects of non-VCS sources observed for VLBI astrometry, and many of the VCS and ICRF sources included in the VLBA calibrator catalogue.

We fitted the provided visibility amplitude  $S(\nu, B)$  at each band to the following Gaussian function:

$$S(\nu, B) = S_0(\nu) \exp[-2(\pi\nu B\delta(\nu)/c)^2], \quad (30)$$

where  $S_0(\nu)$  and  $\delta(\nu)$  are fitting parameters representing flux density with zero baseline and the size of the VLBI component, respectively. If the FITS-IDI data was found for a source in 2005f\_astro, the visibility amplitude versus projected baselines were fitted to equation (30) to estimate  $S_0$  and  $\delta$ . If it wasn't, we referred to the VLBA calibrator catalogue to use the integrated map flux density as  $S_0$ , and the unresolved map flux density as the visibility amplitude obtained with an 8000-km baseline. To extrapolate  $S_0$  and  $\delta$  at 22 and 43 GHz we assumed  $\delta \propto \nu^{-\alpha}$  (Cao and Jiang 2002) and  $S_0 \propto \nu^{-\beta}$ , where  $\alpha$  and  $\beta$  were determined by fitting the *S*-band and the *X*-band results. We then inferred the visibility amplitude with a 25000-km projected baseline from equation (30). If there were multi-epoch FITS-IDI data for a source in 2005f\_astro, we chose the largest value as the expected flux density at each VSOP-2 observing frequency band. If *S*-band data was not available for a source, only the 8.4-GHz estimate for a space baseline was made. If *X*-band data was not available for a source, none of the estimates was made.

Figure 18 shows the distribution of the calibrator candidates with inferred flux densities larger than 50, 60, and

100 mJy at 8.4, 22, and 43 GHz, respectively. The number of candidates decreases as the observing frequency increase. Based on the calibrator candidate distribution, Monte Carlo simulations were performed to estimate the probability to find an adjacent phase referencing calibrator. The sky coverage for the Monte Carlo simulations was restricted to the northern sky because of the lack of the deep southern VLBI catalogue. The maximum separation angles to search for a calibrator were 5°, 3°, and 2° at 8.4, 22, and 43 GHz, respectively. Our Monte Carlo simulations showed that the probabilities are 86, 43, and 20% at 8.4, 22, and 43 GHz, respectively. The requirements for the calibrators and the simulation results are summarized in table 6. At 8.4 GHz, such a high probability is expected for VSOP-2 phase referencing. The probabilities decrease as the frequency increases, because the requirements of the separation angle and flux density become greater. Since the Gaussian fitting of the visibility amplitude as a function of the projected baseline was conducted at the same frequency, we are confident that VSOP-2 phase referencing at 8.4 GHz is promising from the viewpoint of the calibrator availability. Observation chances with phase referencing at 22 and 43 GHz, however, will be restricted in VSOP-2. On the other hand, the result at 22 and 43 GHz will be inspected more carefully because we adopted simple assumptions of  $S_0$  and  $\delta$  to estimate the probabilities.

At 22 and 43 GHz, more sophisticated phase calibration schemes may be needed in addition to phase referencing to circumvent less calibrator availability in VSOP-2. One of the solutions is to observe with fainter calibrators. Assuming a terrestrial radio telescope with a 100-m diameter, calibrators with the flux densities of about 50 mJy will be available at 43 GHz. We conducted another Monte Carlo simulation at 43 GHz with the minimum calibrator flux density of 50 mJy and found that the probability was improved from 20% to 25%. However, because large telescopes can switch the sources much more slowly, it is not effective to use large telescopes in phase referencing at higher observing frequency bands. Doi et al. (2006) showed another possibility to use faint calibrators in phase referencing: they demonstrated their well-organized phase referencing observations, called bigradient phase referencing, using a combination of a very closely located faint calibrator and another bright but rather separate calibrator. Fringes of the target and faint calibrator are detected using the phase referencing technique with the bright calibrator. The long-term phase variations, because of the separation to the bright calibrator, are then calibrated with the closely located calibrators. Although their demonstrations were made at the *X*-band, the proposed method is promising for VSOP-2 at the higher observing frequency bands. A phase-calibration technique with a water vapor radiometer (WVR) is also expected to use fainter calibrators in phase referencing. In this method a WVR is mounted on a terrestrial telescope to measure the amount of water vapor along the line of sight. An example of the successful application of this method is described by Marvel, Woody (1998). The WVR phase calibration tech-

<sup>6</sup> <<http://www.vlba.nrao.edu/astro/calib/vlbaCalib.txt>>.

<sup>7</sup> <[http://vlbi.gsfc.nasa.gov/solutions/2005f\\_astro/](http://vlbi.gsfc.nasa.gov/solutions/2005f_astro/)>.

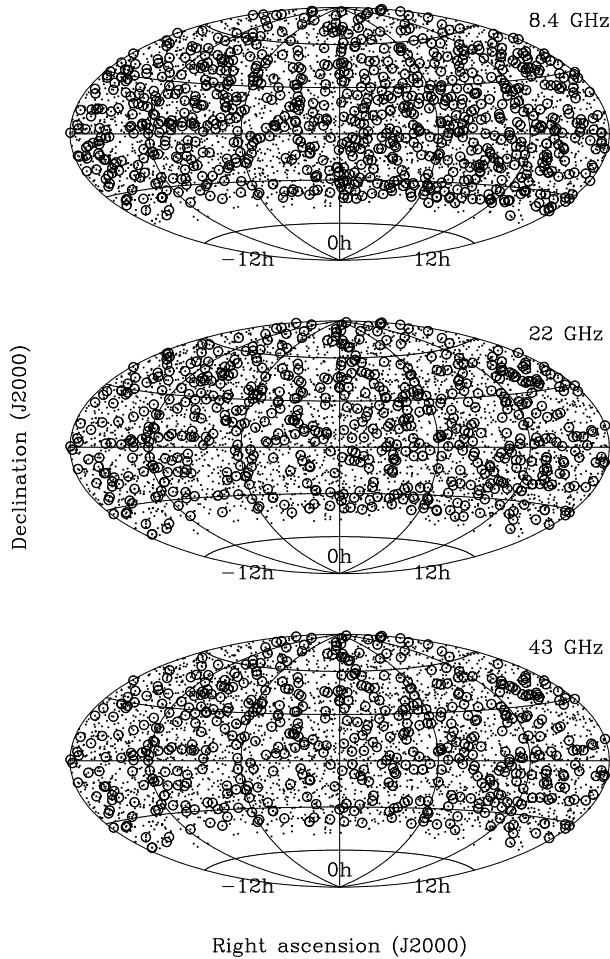


**Fig. 18.** Calibrator candidates for VSOP-2 phase referencing inferred from VLBI surveys at *S*-band and *X*-band. Dots represent sources used in the analysis. The open circles represent calibrator candidates with inferred flux densities for a projected baseline of 25000 km larger than 50, 60, and 100 mJy at 8.4, 22, and 43 GHz, respectively.

nique will be able to achieve longer switching cycle time by removing the tropospheric phase fluctuations. This leads to longer scan durations for both target and calibrator in phase referencing observations, so that we can obtain a higher signal-to-noise ratio for faint calibrators. A longer switching cycle time provides further support to use large terrestrial telescopes with rather slow slew speeds.

Another solution is to observe calibrators at lower frequency bands where a larger number of calibrator candidates is available. The refractivity of the water vapor is almost constant (non-dispersive) for radio waves. Thus, tropospheric phase fluctuations can be calibrated between different frequencies (Asaki et al. 1998). VLBI phase referencing experiments with different frequencies between two sources have been successfully demonstrated by Middelberg et al. (2005). However, since the ionospheric excess path delay is dispersive, it is not possible to correct the ionospheric phase errors with calibrator phases at different frequencies (Rioja et al. 2005). Additional

ARIS simulations were conducted for this multi-frequency phase referencing, and it was found that this method works for the observing frequency combination of 43 and 22 GHz for the target and calibrator, respectively. On the other hand, when calibrator's frequency is 8.4 GHz, large phase offset and fluctuated time variation remain in the compensated 22- or 43-GHz fringe phases due to the ionospheric excess path delays. We have to note that, during summer nights, much larger TEC disturbances than the 50-percentile amplitude are often observed, as indicated in figure 3. It should also be noted that the influence of the ionosphere may be severer than expected above, because the solar activity is likely to reach its maximum in about 2012, when the VSOP-2 satellite is planned to be launched. The above methods introduced here can improve the effectiveness of phase referencing under limited situations. It is important to carefully consider which method works most effectively for the target if some of them are available.

### 5.2. Satellite Attitude Control

Phase referencing has been quite successful when a pair of sources are so close that both of them are observed in the same beam of each radio telescope. In such very fortuitous cases the formal errors of the relative position measurements are as low as several  $\mu\text{as}$  (e.g., Marcaide, Shapiro 1983; Sudou et al. 2003). Since HALCA does not have an ability to change the antenna pointing so quickly, a so-called in-beam phase referencing has been carried out in VSOP (Bartel, Bietenholz 2000; Porcas et al. 2000; Guirado et al. 2001).

A technical challenge in the attitude control of the satellite will be made in VSOP-2 to provide a powerful solution for regularly switching maneuvering. For phase referencing at 43 GHz the satellite is required to repeatedly maneuver between two celestial sources separated by a few degrees every a few tens of seconds, and observe sources with an attitude stability of  $0.005^\circ$ . Since such a switching maneuvering is hardly achievable with standard satellite reaction wheels (RWs), two control moment gyros (CMGs) with a single-gimbaled flywheel spinning at a constant angular rate are planned to be added for fast attitude switching. A CMG is a momentum-exchange device that can produce large output torque on the satellite body by rotating the gimbal axes. The switching maneuvers around the two orthogonal axes for a pair of sources (roll and pitch) are made by controlling the torques provided by the two CMGs while four RWs mainly control the attitude around the axis to the sources (yaw) by generating control torques. The switching maneuvers during a phase referencing observation are the round trip between a pair of sources, so that the two CMGs generate the torques to switch back and forth with no net change in the total angular momentum of the CMG system by an operational symmetry. Numerical simulations for the rigid body with the CMGs showed that a  $3^\circ$  switching maneuver within 15 seconds and tracking the sources during a scan is possible for the 60-s switching cycle time together with a wide range gyroscope. An antenna dynamical model has also



been developed in a feasibility study of the switching maneuvering because the deployable main reflector and boom connecting the reflector and satellite body will be major sources to excite eigen-frequencies causing the attitude disturbance. The satellite will be designed so as not to excite the eigen-frequencies lower than 0.25 Hz for stabilizing the pointing between the switching maneuvers.

A high-speed maneuvering capability with the RWs is important to increase the efficiency of the operation of the space VLBI. The capability of the attitude maneuvering over large angles with a rate of  $0^\circ.1 \text{ s}^{-1}$  will also be useful for fringe-finder scans interleaved in a phase referencing observation.

### 5.3. Highly Accurate Orbit Determination

A highly accurate OD, with a positional accuracy of better than several centimeters, is required for VSOP-2 phase referencing. This requirement is two orders of magnitude better than the OD accuracy achieved for HALCA by Doppler tracking. One of the possible methods to achieve the OD required for VSOP-2 phase referencing is to use the on-board GPS receiver: by using on-board GPS navigation systems, the TOPEX/POSEIDON satellite launched in 1992 to measure the ocean surface level achieved the OD accuracy of 2–3 cm, and GRACE, to measure the center of the gravity of the Earth, achieved an OD accuracy of about 1–2 cm. These satellites are in relatively low-Earth orbits, so that more than several GPS satellites, whose altitudes are  $\sim 20200$  km, are always available. When the user altitude is higher than  $\sim 3500$  km, it will be outside of the main beam illumination of a given GPS satellite, because the beam width of the GPS transmitting antenna is designed to illuminate near-Earth users. At altitudes near the VSOP-2 satellite apogee, zero to only three GPS satellites can be available at any given time, even with the on-board GPS receiver antenna system covering all directions.

To strengthen the orbit determination, high-quality accelerometers can be used together with the GPS measurements. Accelerometry will connect the orbit positions and the velocities over periods of time when the GPS measurements are unable to provide good solutions. Wu, Bar-Sever (2001) showed in their covariance analysis for the VSOP-2 OD that the conventional GPS navigation with accelerometry can achieve an orbit formal error well below 1 cm for the VSOP-2 satellite in all the three components near perigee. At higher altitudes, however, the OD error grows to about 2 cm with the assumption of an on-board accelerometer of  $1 \text{ nm s}^{-2}$  accuracy due to the lack of GPS measurements at these altitudes.

Another possibility is to have a GPS-like signal transmitter on the VSOP-2 satellite. It is expected that, in conjunction with the on-board GPS receiver, the OD accuracy will then be less than 1.5 cm. To further improve the OD accuracy to the 1-cm level, ultra-precise accelerometers at the level of  $0.1 \text{ nm s}^{-2}$  now available should be used. It should be noted that missions like GRACE were carefully designed to have the accelerometer at the center of mass of the satellite, which may be difficult to achieve

**Table 6.** Probabilities to find a suitable calibrator for VSOP-2 phase referencing.

	8.4 GHz	22 GHz	43 GHz
$S^c$	$\geq 50 \text{ mJy}$	$\geq 60 \text{ mJy}$	$\geq 100 \text{ mJy}$
$\Delta\theta$	$\leq 5^\circ$	$\leq 3^\circ$	$\leq 2^\circ$
Probability*	86%	43%	20%

\* Monte Carlo simulations were performed for the northern sky.

for the VSOP-2 satellite. To assure the 1-cm accuracy at all times, better determination of GPS orbits and clocks will be required.

Galileo is a GPS-like navigation system planned in Europe, to be fully operational in 2008. The constellation consists of 30 satellites whose orbits are the circular with the altitude of 23616 km. Galileo satellites will be equipped with the hydrogen maser time standards and are expected to achieve more precise OD. This system is more effective for VSOP-2 and the 2.5-cm level OD can be achieved only with the use of GPS/Galileo receivers on the VSOP-2 satellite.

## 6. Conclusions

The effectiveness of phase referencing with VSOP-2 was verified in detail with a newly developed software simulation tool, ARIS. Simulations with ARIS show that phase referencing with VSOP-2 is promising at 8.4 GHz for all of the tropospheric conditions, while at 22 and 43 GHz the phase referencing observations are recommended to be conducted under good and typical tropospheric conditions. At 22 and 43 GHz there is another difficulty in terms of the calibrator choice: our ARIS simulations show that it is safe to choose a phase referencing calibrator with the expected signal-to-noise ratio on a space baseline larger than 4 for a single calibrator scan, but such a bright calibrator cannot always be found closely enough to a given target at 22 and 43 GHz.

The specification requirements of the satellite in terms of the maneuvering capability and OD were obtained from our investigations. At 22 and 43 GHz, one-minute or shorter switching capability is required, while a few minute or longer switching cycle times may be used at 8.4 GHz. An accuracy of the orbit determination of less than  $\sim 10$  cm is required for the mission. Current studies concerning the VSOP-2 satellite design indicate prospects that it is not easy, but not impossible, to achieve.

Although the atmospheric systematic errors cannot perfectly be removed with the a priori values calculated in the correlator, those phase errors can be corrected in well-organized phase referencing observations along with multiple calibrators. Note that the satellite does not need to observe multiple calibrators in a short period, because the systematic errors are related to the terrestrial telescopes. If the atmospheric systematic errors can be successfully removed, a few centimeter OD accuracy will be targeted so that the performance of VSOP-2 phase referencing will be greatly improved.

In this report we have demonstrated the usefulness of ARIS in investigating the effectiveness of VSOP-2 phase referencing. ARIS will also be convenient to check VLBI observation plans from the viewpoint of image quality. In this report we considered some of the intended cases of VSOP-2 phase referencing observations for point sources with the highest spatial resolution; further investigation can be made for an individual source. This is important for the VSOP-2 scientific goals, especially at 22 and 43 GHz, because the phase referencing technique cannot always be used at those frequency bands in terms of finding calibrators. ARIS will give helpful suggestions to comprise the effective observation and operation plans for the best performance in VSOP-2.

The authors made use of the GPS TEC data taken by GSI and provided by Kyoto University. The authors made use of the VLBA calibrator catalogue of NRAO and 2005f\_astro catalogue of NASA GFSC. The authors express their hearty thanks to all members of VSOP-2 project team, especially, H. Hirabayashi of ISAS who is leading the next space VLBI working group and M. Inoue of NAOJ space VLBI project office. The authors also express their thanks to S-C. Wu and Y. Bar-Sever of the Jet Propulsion Laboratory for their investigations of the VSOP-2 satellite OD. Y. Asaki gives his thanks to T. Ichikawa of ISAS for useful suggestions about the satellite OD, K. Noguchi of Nara women's university for discussion about the ionospheric TEC fluctuations, and L. Petrov of NASA GSFC for discussion about the VLBI compact radio source surveys, and D. Jauncey for comments about this work.

## References

- Asaki, Y., Saito, M., Kawabe, R., Morita, K-I., & Sasao, T. 1996, *Radio Sci.*, 31, 1615
- Asaki, Y., Shibata, K. M., Kawabe, R., Roh, D-G., Saito, M., Morita, K-I., & Sasao, T. 1998, *Radio Sci.*, 33, 1297
- Bartel, N., Herring, T. A., Ratner, M. I., Shapiro, I. I., & Corey, E. 1986, *Nature*, 319, 733
- Bartel, N., & Bietenholz, M. F. 2000, in *Astrophysical Phenomena Revealed by Space VLBI*, ed. H. Hirabayashi, P. G. Edwards, & D. W. Murphy (ISAS, Sagami-hara), 17
- Beasley, A. J., & Conway, J. E. 1995, in *Very Long Baseline Interferometry and the VLBA*, ed. J. A. Zensus, P. J. Diamond, & P. J. Napier (ASP Conf. Ser., 82), 327
- Beasley, A. J., Gordon, D., Peck, A. B., Petrov, L., MacMillan, D. S., Fomalont, E. B., & Ma, C. 2002, *ApJS*, 141, 13
- Bristow, W. A., & Greenwald, R. A. 1997, *J. Geophys. Res.*, 102, 11585
- Brunthaler, A., Reid, M. J., Falcke, H., Greenhill, L. J., & Henkel, C. 2005, *Science*, 307, 1440
- Carilli, C. L., & Holdaway, M. A. 1999, *Radio Sci.*, 34, 817
- Cao, X., & Jiang, D. R., 2002, *MNRAS*, 331, 111
- Cotton, W. D. 1995, in *Very Long Baseline Interferometry and the VLBA*, ed. J. A. Zensus, P. J. Diamond, & P. J. Napier (ASP Conf. Ser., 82), 189
- Doi, A., et al. 2006, *PASJ*, 58, 777
- Dravskikh, A. F., & Finkelstein, A. M. 1979, *Ap&SS*, 60, 251
- Fey, A. L., et al. 2004, *AJ*, 127, 3587
- Fomalont, E. 1995, in *Very Long Baseline Interferometry and the VLBA*, ed. J. A. Zensus, P. J. Diamond, & P. J. Napier (ASP Conf. Ser., 82), 363
- Fomalont, E. B., Petrov, L., MacMillan, D. S., Gordon, D., & Ma, C. 2003, *AJ*, 126, 2562
- Gallimore, J. F., & Beswick, R. 2004, *AJ*, 127, 239
- Gallimore, J. F., Baum, S. A., & O'Dea, C. P. 2004, *ApJ*, 613, 794
- Georges, T. M. 1968, *Journal of Atmospheric and Terrestrial Physics*, 30, 735
- Guirado, J. G., Ros, E., Jones, D. L., Lestrade, J. -F., Marcaide J. M., Pérez-Torres, M. A., & Preston, R. A. 2001, *A&A*, 371, 766
- Gwinn, C. R., Taylor, J. H., Weisberg, J. M., & Rawley, R. A. 1986, *AJ*, 91, 338
- Hirabayashi, H., et al. 1998, *Science*, 281, 1825
- Hirabayashi, H., et al. 2000, *PASJ*, 52, 955
- Hirabayashi, H., et al. 2004, *Proc. SPIE*, 5487, 1646
- Ho, C. M., Wilson, B. D., Mannucci, A. J., Lindqwister, U. J., & Yuan, D. N. 1997, *Radio Sci.*, 32, 1499
- Lestrade, J. -F., Rogers, A. E. E., Whitney, A. R., Niell, A. E., Phillips, R. B., & Preston, R., 1990, *AJ*, 99, 1663
- Ma, C., et al. 1998, *AJ*, 116, 516
- Marcaide, J. M., & Shapiro, I. I. 1983, *AJ*, 88, 1133
- Marvel, K. B., & Woody, D. P. 1998, *Proc. SPIE*, 3357, 442
- McCarthy, D. D., & Petit, G. (ed.) 2004, *IERS Technical Notes*, 32, ch.5
- Middelberg, E., et al. 2005, *A&A*, 433, 897
- Migenes, V., et al. 1999, *ApJS*, 123, 487
- Murphy, D., Preston, R., Fomalont, E., Romney, J., Ulvestad, J., Greenhill, L., & Reid, M. 2005, in *Future Directions in High Resolution Astronomy*, ed. J. D. Romney, & M. J. Reid (ASP Conf. Ser., 340), 575
- Napier, P. J. 1995, in *Very Long Baseline Interferometry and the VLBA*, ed. J. A. Zensus, P. J. Diamond, & P. J. Napier (ASP Conf. Ser., 82), 59
- Niell, A. E. 1996, *J. Geophys. Res.*, 101, 3227
- Noguchi, K., Imamura, T., Oyama, K-I., & Saito, A. 2001, *Radio Sci.*, 36, 1607
- Petrov, L., Kovalev, Y. Y., Fomalont, E., Gordon, D. 2005, *AJ*, 129, 1163
- Petrov, L., Kovalev, Y. Y., Fomalont, E. B., Gordon, D. 2006, *AJ*, 131, 1872
- Porcas, R. W., Rioja, M. J., Machalski, J., & Hirabayashi, H. 2000, in *Astrophysical Phenomena Revealed by Space VLBI*, ed. H. Hirabayashi, P. G. Edwards, & D. W. Murphy (ISAS, Sagami-hara), 245
- Pradel, N., Charlot, P., & Lestrade, J.-F. 2006, *A&A*, 452, 1099
- Reid, M. J., Readhead, A. C. S., Vermeulen, R. C., & Treuhaft, R. N. 1999, *ApJ*, 524, 816
- Rioja, M., Dodson, R., Porcas, R., Suda, H., & Colomer, F. 2005, in *Proceedings of the 17th working meeting on European VLBI for geodesy and astrometry*, ed. M. Vennebusch, & A. Nothnagel (INAF Istituto di Radioastronomia Sezione di NOTO, Italy), 125
- Ros, E., Marcaide, J. M., Guirado, J. C., Sardón, E., & Shapiro, I. I. 2000, *A&A*, 356, 357
- Saito, A., Fukao, S., & Miyazaki, S. 1998, *Geophys. Res. Lett.*, 25, 3079
- Shapiro, I. I., et al. 1979, *AJ*, 84, 1459
- Smith, K, Pestalozzi, M., Güdel, M., Conway, J., & Benz, A. O. 2003, *A&A*, 406, 957

- Sudou, H., Iguchi, S., Murata, Y., & Taniguchi, Y. 2003, Science, 300, 1263
- Tatarskii, V. I. 1961, Wave Propagation in a Turbulent Medium (Dover, New York), ch.1
- Thompson, A. R., Moran, J. M., & Swenson, Jr., G. W. 2001, Interferometry and synthesis in radio astronomy (A Wiley-Interscience Publication, John Wiley & Sons, Inc., New York), ch.13
- Treuhaff, R. N., & Lanyi, G. E. 1987, Radio Sci., 22, 251
- Wu, S-C., & Bar-Sever, Y. 2001, Proc. ION GPS 2001 (Salt Lake City, Utah), 2272